JOURNAL OF PETROLOGY | VOLUME 44 | NUMBER 2 | PAGES 197–225 | 2003

Metamorphic and Tectonic Evolution of the Hwacheon Granulite Complex, Central Korea: Composite *P–T* Path Resulting from Two Distinct Crustal-Thickening Events

SEUNG RYEOL LEE[1] AND MOONSUP CHO[2]*

[1]GEOLOGY DIVISION, KOREA INSTITUTE OF GEOSCIENCE AND MINERAL RESOURCES, TAEJON, 305-350 SOUTH KOREA

[2]SCHOOL OF EARTH AND ENVIRONMENTAL SCIENCES, SEOUL NATIONAL UNIVERSITY, SEOUL, 151-742 SOUTH KOREA

RECEIVED SEPTEMBER 3, 2001; REVISED TYPESCRIPT ACCEPTED JULY 29, 2002

The Hwacheon granulite complex (HGC), occupying the north-eastern margin of the Gyeonggi massif, consists mainly of garnetiferous leucocratic gneiss and leucogranite together with minor kyanite–garnet gneiss, aluminous gneiss, mafic granulite and garnet amphibolite. Mineral assemblages and reaction textures in various rock types of the HGC document five distinct metamorphic stages: pre- (M_1) and peak (M_2) granulite-facies metamorphism; lower temperature, high (M_3) and low (M_4) pressure upper amphibolite-facies metamorphism; and local retrogression (M_5) producing andalusite-bearing assemblages. Each metamorphic stage can be integrated to give a composite P–T *path consisting of two distinct trajectories, characterized by clockwise* P–T *loops at relatively high and low temperatures, respectively. The first* P–T *trajectory (M_1–M_3) corresponds to a Palaeoproterozoic tectonometamorphic event responsible for the formation of the granulite complex at ~1·87 Ga. Rare inclusions of kyanite in M_2 garnet from pelitic granulites suggest an episode of crustal thickening (M_1) before M_2. The peak granulite-facies metamorphism at ~7·0–9·5 kbar and 790–830°C induced widespread partial melting in pelitic granulites and produced syn- to post-tectonic, (para-)autochthonous leucogranites. An episode of quasi-isobaric cooling (M_3) following the M_2 event is apparent from the occurrence of garnet coronas around orthopyroxene in mafic granulites and kyanite replacing sillimanite in pelitic granulites. The heat required for granulite formation is attributed to the burial of sedimentary protoliths rich in radiogenic elements during the Palaeoproterozoic crustal-thickening event. The second* P–T *trajectory (M_4) is correlated with the final exhumation of the HGC. This decompressional process, probably initiated in the kyanite stability field, reached pressures of ~3–6 kbar at 660–750°C. The clockwise* P–T *path may reflect the exhumation of a deep-seated crustal segment along discrete, ductile shear zones during the Permo-Triassic collisional orogeny prevalent in Far-East Asia.*

KEY WORDS: *crustal thickening; granulite; Gyeonggi massif; Korea metamorphism*

INTRODUCTION

Metamorphic rocks contain a variety of clues for understanding the ancient thermal structure and evolution of the continental crust, and the delineation of pressure–temperature histories of such rocks provides some constraints on the associated tectonic processes (e.g. Thompson & Ridley, 1987; Harley, 1989; Brown, 1993). Exposed granulite-facies terranes are commonly regarded as windows into the middle to lower continental crust (e.g. Fountain & Salisbury, 1981; Percival *et al.*, 1992). Thus, investigations on the pressure–temperature paths of granulites help us to evaluate the deep crustal processes

*Corresponding author. E-mail: moonsup@snu.ac.kr

responsible for formation and stabilization of the continental crust.

In most granulite-facies terranes, chemical and textural evidence from the prograde stage of metamorphism is eradicated during subsequent recrystallization at peak metamorphic conditions. As a result, quantitative data are generally available only for the retrograde portion of the P–T path (e.g. Bohlen, 1987; Harley, 1989). In this respect, mineral inclusions and reaction textures, such as coronas or reaction rims, provide additional constraints for delineating the pressure–temperature–time (P–T–t) path, because they reflect textural readjustment to changes in pressure and temperature. On the basis of reaction textures supplemented by geothermobarometric data, near-isothermal decompression (ITD) or near-isobaric cooling (IBC) paths have been identified as two end-member situations for the thermo-tectonic evolution of granulite-facies terranes (e.g. Harley, 1989). These P–T–t paths are often assumed to be the product of single metamorphic episodes when inferring the tectonic setting of granulite formation. However, because dry rocks such as granulites are likely to undergo significant recrystallization only during deformation and/or fluid influx, mineral assemblages and reaction textures in such rocks may represent segments of P–T paths that are unrelated in time (e.g. Harley, 1992). As a consequence, these segments cannot be used to construct a realistic P–T–t path, unless reliable ages are available (Hensen *et al.*, 1995; Vernon, 1996). Such composite P–T paths could be common for Precambrian granulite-facies terranes, especially in the context of the timing and nature of granulite exhumation with respect to granulite formation (Percival *et al.*, 1992). Exhumation of granulite-facies terranes may occur through their involvement in a separate tectonic event sometime after their high-T formation (Ellis, 1987; Harley, 1989). Thus, reaction textures in granulites may not reflect a single metamorphic episode recording a single P–T–t path (see Hollister & Crawford, 1986).

The Hwacheon granulite complex (HGC), a coherent region of granulites, has been identified in the northeastern margin of the Gyeonggi massif, South Korea (Figs 1 and 2; Lee *et al.*, 1997, 2000). This complex formed at ~1·87 Ga (Lee *et al.*, 2000), and represents the middle to lower crust of the Gyeonggi massif. The HGC preserves various mineral parageneses and reaction textures that allow the construction of a reliable P–T path. Accordingly, the Hwacheon granulites provide a good opportunity for improving our understanding of deep crustal processes with regard to granulite formation and its reactivation in central Korea. In this study, we have investigated the P–T evolution of the HGC, on the basis of mineral parageneses deduced from various reaction textures as well as geothermobarometric data on both mafic and pelitic granulites. These results are combined with available geochronologic data to unravel the timing and nature of granulite formation and subsequent reactivation. Finally, the elucidation of a P–T–t path for the HGC provides some insight into the geodynamic processes that governed the tectonometamorphism of basement rocks in not only the Korean Peninsula but also Far-East Asia as a whole.

GENERAL GEOLOGY

The Gyeonggi massif, situated between the Nangrim and Yeongnam massifs of the Korean Peninsula (Fig. 1), is a Precambrian terrane consisting primarily of Archaean to Palaeoproterozoic crystalline basement and Palaeo- to Mesoproterozoic supracrustal rocks (Fig. 1; Lee, 1987). The Gyeonggi massif has been regarded as an eastern promontory of the South China (or Yangtze) craton, and the Nangrim and Yeongnam massifs as parts of the Sino-Korean craton (Cluzel *et al.*, 1991; Yin & Nie, 1993; Li, 1994; Ree *et al.*, 1996; Chough *et al.*, 2000; Kim *et al.*, 2000; Lee *et al.*, 2000). Hence, both northern and southern margins of the Gyeonggi massif are considered as tectonic boundaries. However, the geodynamic processes responsible for the amalgamation of Precambrian massifs in Korea are poorly understood.

We have previously reported the occurrence of a coherent granulite terrane in the Hwacheon area, which forms part of the northeastern Gyeonggi massif (Fig. 1; Lee *et al.*, 1997, 2000). On the basis of lithology and field relationships, two lithotectonic units are distinguished: the Hwacheon granulite complex (HGC) and the marginal zone gneiss complex (MZGC) (Fig. 2). The HGC occurs as a tectonically exhumed block, separated from the MZGC by thrust faults and ductile shear zones. The southward-directed thrust emplacement of the HGC over the MZGC produced intense folding in the MZGC, and was followed by extensional shearing focused along the boundary between the HGC and the MZGC. The latter is interpreted to result from gravitational collapse of the thickened crust (Lee *et al.*, 2000). It should be noted that the majority of structural fabrics observed are not associated with the formation of the granulites but rather with their exhumation.

The HGC is a composite migmatite complex that has experienced granulite-facies metamorphism and partial melting of pelitic and psammopelitic rocks. Thus, this complex belongs to a metatexite–diatexite terrane, following the definitions of Brown (1973). The HGC consists primarily of garnetiferous leucocratic gneiss and leucogranite together with subordinate kyanite–garnet gneiss, aluminous gneiss, mafic granulite, and garnet amphibolite. Pelitic granulites include leucocratic gneiss as well as kyanite–garnet and aluminous gneisses. The leucogranites or the leucosomes in migmatitic granulites

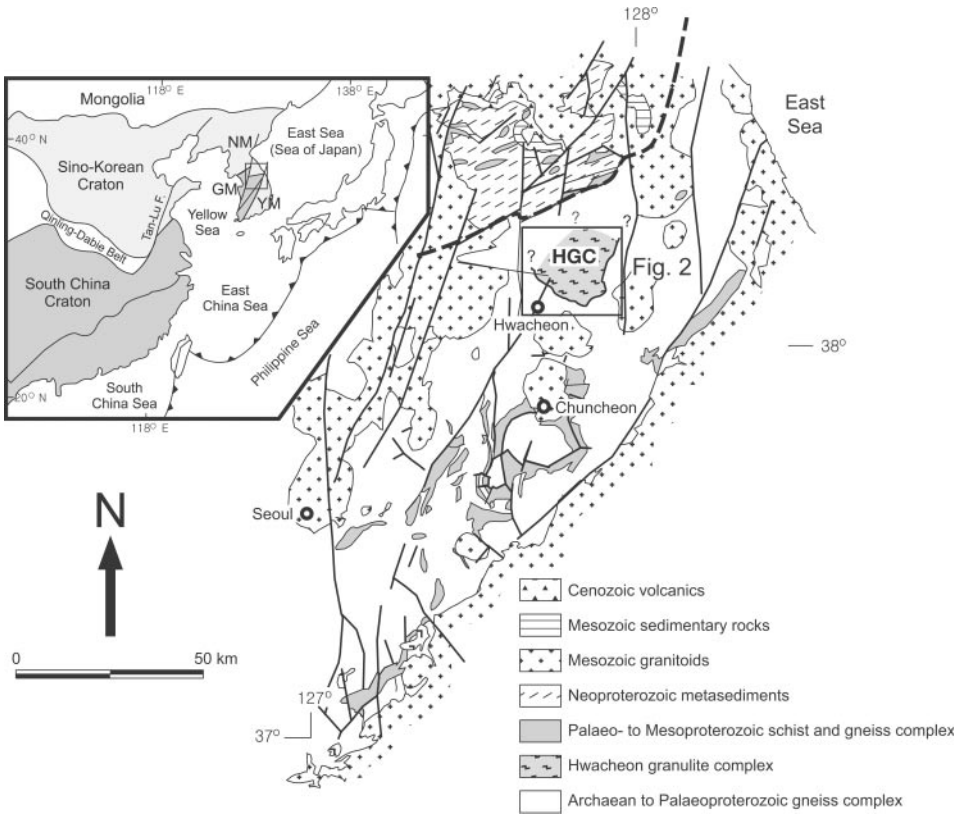

Fig. 1. A simplified geological map of the eastern Gyeonggi massif. Location of the study area, including the Hwacheon granulite complex (HGC), is shown as a box. The dashed line represents the approximate boundary between the Gyeonggi and Nangrim massifs. Inset figure is a tectonic province map of East Asia. NM, Nangrim massif; GM, Gyeonggi massif; YM, Yeongnam massif.

contain grains or clusters of garnet, and are probably crystallized from *in situ* or para-autochthonous partial melts. They commonly occur as layers conformable with the foliation or as irregular patches filling tension gashes (Fig. 3a and b), together with garnet-rich rafts or layers in metatexitic regions. Metatexitic migmatite is locally transformed into diatexite containing rare patches of garnet-rich residue (Fig. 3c). The melt-enriched diatexite is considered to be the source of para-autochthonous granite occurring as large massive bodies in the HGC and MZGC (Figs 2 and 3d). Blocks or layers of kyanite–garnet gneiss are commonly enclosed by the diatexite and closely associated with leucosomes (Fig. 3e). Aluminous gneiss is equivalent in lithology to the garnet-rich residue observed in the metatexite, but occurs as a mappable body (Fig. 3f). This gneiss is considered to be the product of extensive partial melting, and to be complementary to the diatexite. The igneous protoliths of the mafic granulites were apparently emplaced before the granulite-facies metamorphism, although their temporal relationships are often ambiguous as a result of structural disturbance during partial melting. The occurrence of mafic granulite is restricted to the HGC, whereas garnet amphibolites are present in both the HGC and the MZGC. Widespread partial melting has apparently occurred after the major deformation, because the diatexites show no penetrative fabric.

The MZGC represents a northern extension of the Gyeonggi metamorphic complex (GMC) in the central Gyeonggi massif, and consists of banded biotite gneiss, quartzofeldspathic gneiss and migmatitic gneiss together with minor amphibolite (Lee, 1987; Lee & Cho, 1995). Because of its lithologic similarity, the migmatitic gneiss of the MZGC is tentatively interpreted as the lower-grade or retrogressive equivalent of leucocratic gneiss in the HGC. A conventional U–Pb zircon age of 2164 $\pm$ 18 Ma was reported from banded gneiss in the MZGC (Kim *et al.*, 1999). On the other hand, the protoliths of garnet amphibolites that underwent near-isothermal decompression along a clockwise *P–T–t* path were emplaced during Neoproterozoic (852 $\pm$ 48 Ma) time (Lee & Cho, 1995). Thus, the maximum age for regional metamorphism in the MZGC should be younger than $\sim$850 Ma.

PETROGRAPHY

Mineral parageneses in representative leucocratic and aluminous gneisses, kyanite–garnet gneiss, mafic gran-

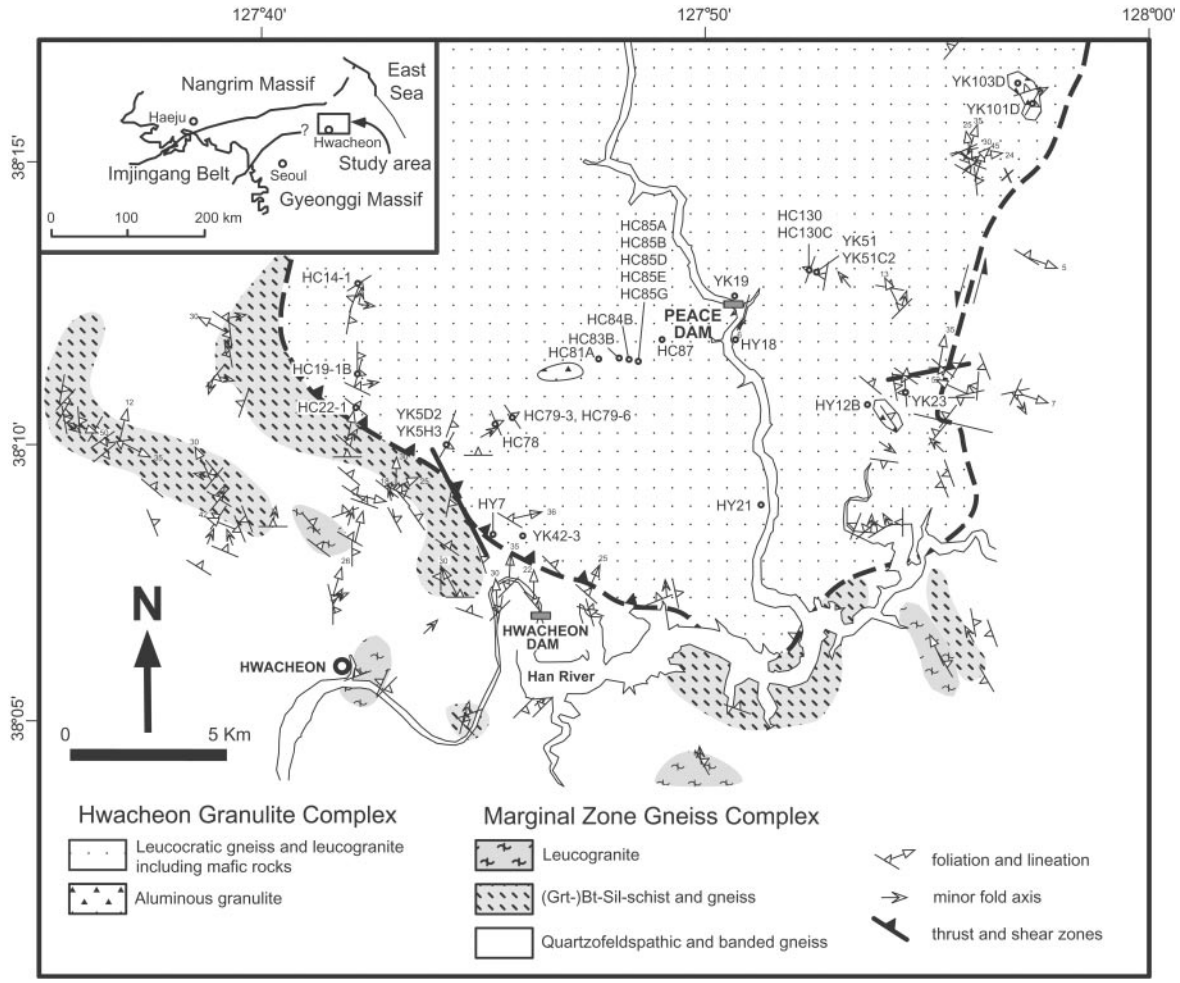

Fig. 2. A schematic geological map of the study area [modified after Lee *et al.* (1997, 2000)], showing locations of the analyzed samples. Inset figure shows the location of the study area and the Imjingang belt [adapted after Cho *et al.* (1995)].

ulites and amphibolites are summarized in Table 1. Although the granulite-facies assemblages are dominant in all lithologic units, each unit partially preserves textural evidence for mineral growth during pre- and post-peak metamorphic stages. Mineral parageneses recorded in various rock types suggest that the HGC has experienced five metamorphic stages, M_1 to M_5 (Table 1). Among them, M_2 defines the peak granulite-facies metamorphism, whereas M_1 minerals are present only as inclusions in M_2 porphyroblasts. M_3 and M_4 represent high- and low-P upper amphibolite-facies stages, respectively. M_5 represents a local thermal overprint associated with intrusion of Jurassic plutons.

In particular, three generations of garnet are distinguished during polymetamorphic evolution of the HGC. The majority of garnet grains are formed during M_2 peak metamorphism, but texturally later garnet growths are characteristic for the M_3 and M_4 stages in mafic and pelitic granulites, respectively (Table 1). Moreover, M_3 garnet grains in mafic granulites are thought to be a retrograde product, whereas texturally late garnet growths in pelitic granulites are attributed to an even later, prograde M_4 event (see below for further discussion).

Leucocratic gneiss and leucogranite

The leucocratic gneisses are commonly layered, and occur as isolated blocks or rafts in the diatexitic region dominated by garnet-bearing leucogranite. Mafic layers of the leucocratic gneiss are generally rich in residual garnet and biotite, and are considered to represent a restitic portion, from which felsic melts have been segregated or extracted. The leucogranites contain lesser amounts of biotite than the leucocratic gneisses. Primary mineral assemblages of leucocratic gneisses and leucogranites are represented by garnet–sillimanite–biotite–K-feldspar–plagioclase–quartz. Primary

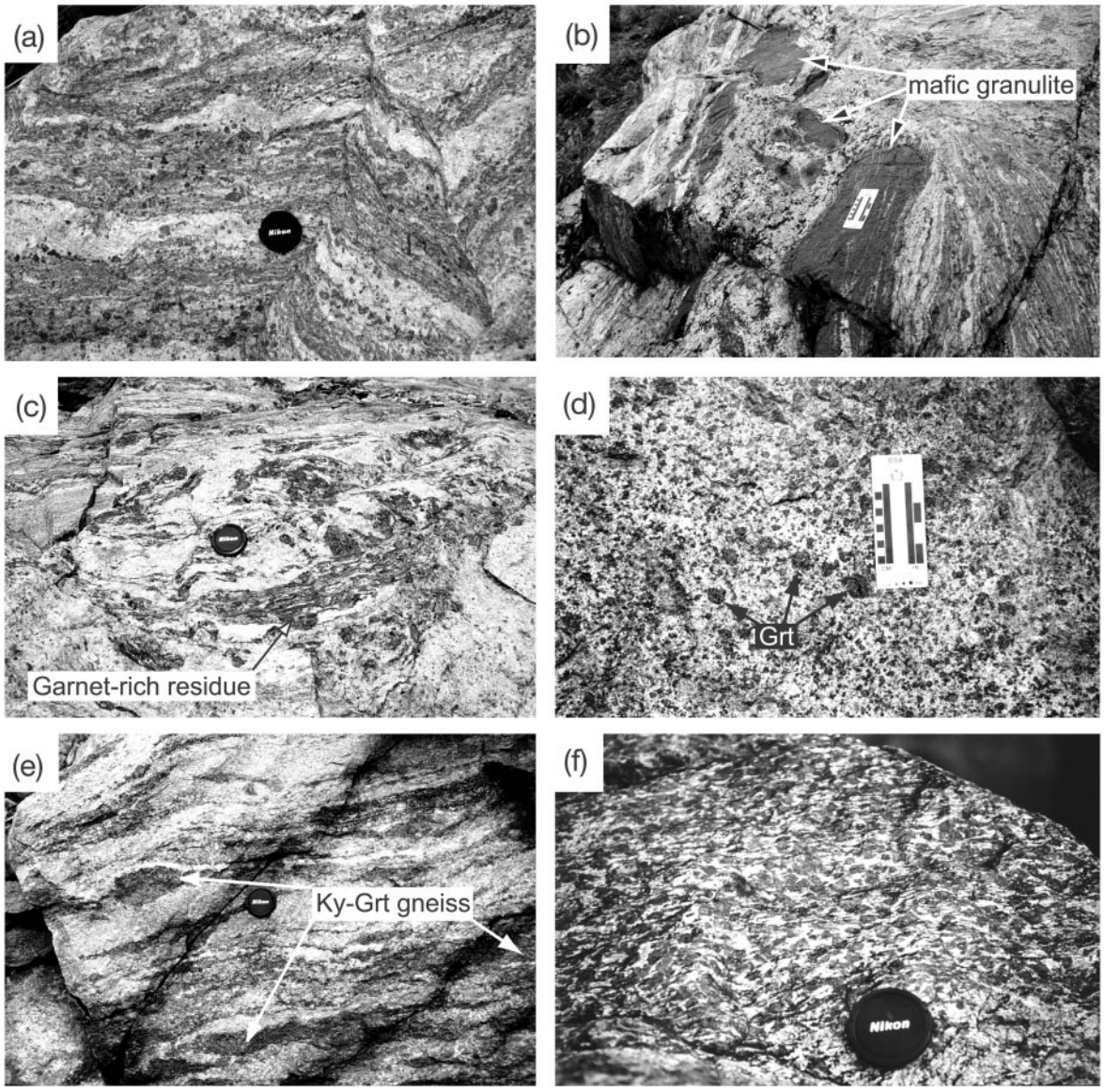

Fig. 3. Outcrop photographs showing various lithologies in the HGC. (a and b) Metatexitic migmatites: (a) stromatic structures are preserved in garnetiferous leucocratic gneiss; (b) garnet-bearing leucogranites occur as concordant layers and small patches filling the boudinaged necks of mafic granulites. (c) Diatexitic migmatite containing garnet-rich rafts or melanosomes that are disrupted or isolated by leucogranites. (d) Garnet-bearing leucogranite showing no distinct compositional layers. The size of garnet grains reaches several centimetres. (e) Kyanite–garnet gneiss occurring as concordant layers or patches within leucocratic gneiss. (f) Aluminous granulite that appears similar to garnet-rich rafts commonly observed in metatexite and diatexite. Lens cap for scale is 52 mm in diameter.

M_2 garnet occurs as sub- to euhedral porphyroblasts ranging in diameter up to $\sim$10 cm, which commonly enclose biotite, sillimanite, plagioclase, quartz and rare hercynite (Fig. 4a). Sillimanite is the dominant Al-silicate in the leucocratic gneiss and occurs as acicular crystals subparallel to the foliation primarily defined by the preferred orientation of biotite. K-feldspar forms medium-sized to large perthitic poikiloblasts, commonly enclosing biotite, sillimanite and quartz.

M_4 minerals in leucocratic gneisses and leucogranites include cordierite, garnet and hercynite, which commonly coexist with residual biotite (Fig. 4b and c). Cordierite occurs dominantly as a xenoblastic phase that mantles the M_2 garnet porphyroblasts (Fig. 4b), and uncommonly as isolated patches replacing residual biotite. M_4 garnet and hercynite occur in close association with cordierite (Fig. 4c). In leucocratic gneisses (samples HC19-1B and HC85D), rare idioblasts of kyanite are observed in the

Table 1: Mineral assemblages in representative granulite-facies rocks from the Hwacheon granulite complex

Sample no.	Rock type	Grt	Crd	Ky	Sil	And	Ksp	Bt	Pl	Qtz	Hc	St	Opx	Cpx	Hb	Cum	Others
Pelitic rocks																	
HC19-1B	leucocratic gneiss	2		3	x		x	x	x	x							Rt(3), Ilm(x)
HC22-1	leucocratic gneiss	2			x		x	x	x	x	1						Crn(2), Ilm(x)
HC78	leucocratic gneiss	2, 4	4		x		x	x	x	x							Ilm(x)
HC79-3	leucocratic gneiss	2			x		x	x	x	x	1						Ilm(x)
HC79-6	leucocratic gneiss	2			x		x			1							Ilm(x)
HC83B	leucocratic gneiss	2, 4	4		x		x	x	x	x	4						Ilm(x)
HC85D	leucocratic gneiss	2, 4	4	3	x		x	x	x	x	4						Ilm(x)
HC130C	Ky–Grt gneiss	2	4	1, 3	x	5		x	x	x	3	1, 3					Rt(3), Ilm(x)
HY7	leucocratic gneiss	2			x		x	x	x	x							Ilm(x)
HY12B	leucocratic gneiss	2			x		x	x	x	x							Ilm(x)
HY18	leucocratic gneiss	2, 4	4		x		x	x	x	x							Ilm(x)
HY21	leucocratic gneiss	2, 4	4		x		x	x	x	x							Ilm(x)
YK19	leucocratic gneiss	2, 4	4		x		x	x	x	x							Ilm(x)
YK23	leucocratic gneiss	2, 4	4		x		x	x	x	x	3						Crn(3), Ilm(x)
YK42-3	leucocratic gneiss	2, 4	4		x		x	x	x	x							Ilm(x)
YK51B	Ky–Grt gneiss	2	4	3	x			x	x	x	3						Rt(3), Ilm(x)
YK51C2	Ky–Grt gneiss	2	4	3	x			x	x	x	3	3					Rt(3), Ilm(x)
YK101D	aluminous gneiss	2		1, 3	x		x	x	x	x							Rt(3), Ilm(x)
YK103D	aluminous gneiss	2		1, 3	x		x	x	x	x							Rt(3), Ilm(x)
Mafic rocks																	
HC14-1	mafic granulite	2, 3						x	x	x					3	3	Ilm(x)
HC81A	mafic granulite	3							x	x			2	2	3	3	Ilm(x)
HC84B	mafic granulite	3						2	x	x			2	2	2, 3	3	Ilm(x)
HC85A	mafic granulite	2, 3						x	x	x			2			3	Ilm(x)
HC85E	mafic granulite	2, 3						x	x	x			2			3	Ilm(x)
HC85G	mafic granulite	3						2	x	x			2	2	2, 3	3	Ilm(x)
HC87	mafic granulite	2, 3						x	x	x			2		3	3	Ilm(x)
HC130	amphibolite	3							x	x					3		Ilm(x)
YK5D2	mafic granulite	2, 3						x	x	x			2		3	3	Ilm(x)
YK5H3	mafic gneiss	2, 3							x	x				2	3		Ilm(x)

Mineral abbreviations from Kretz (1983). Numbers refer to metamorphic stages of M_1 to M_5. x, a phase possibly present at all stages.

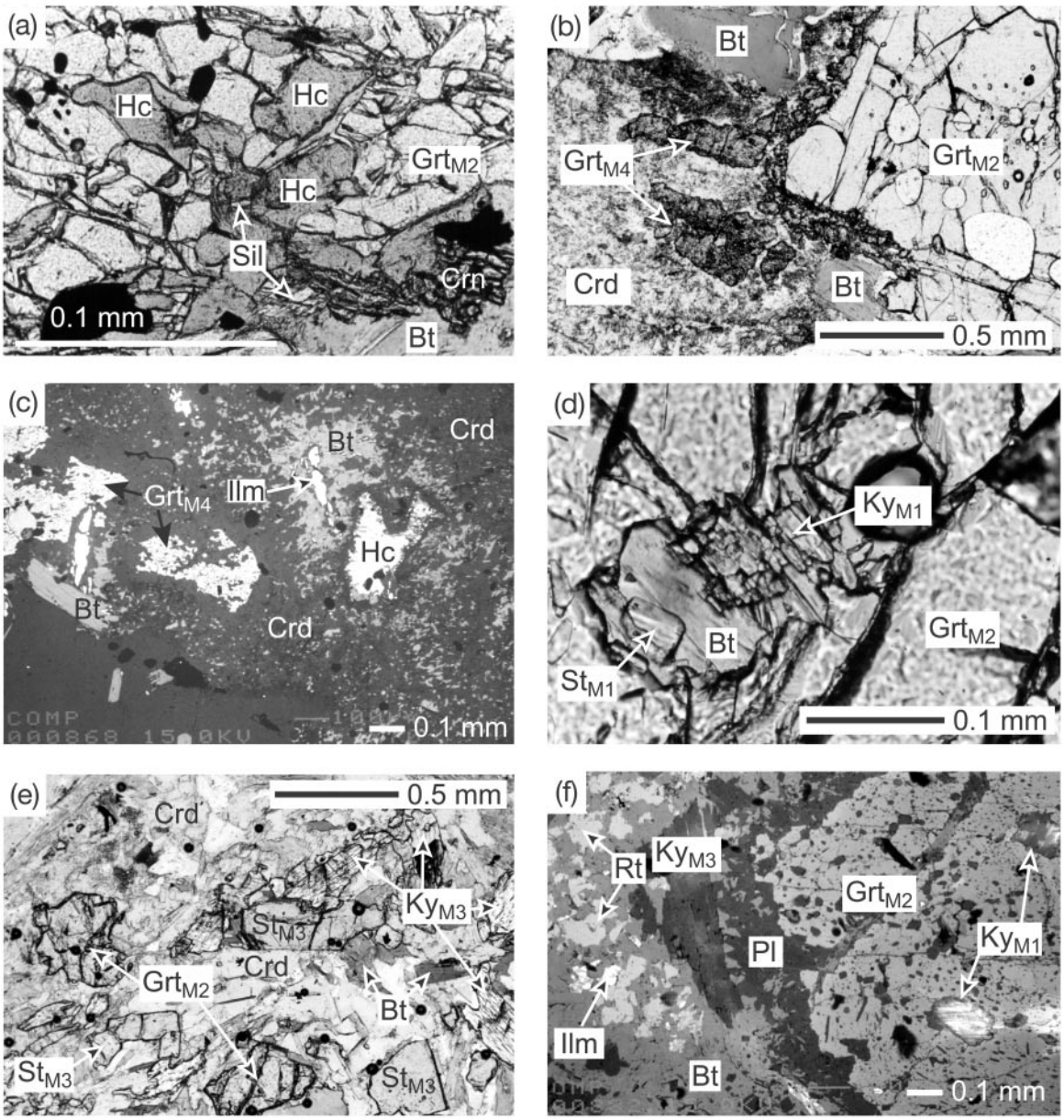

Fig. 4. Photomicrographs and backscattered electron (BSE) images showing various reaction textures in pelitic granulites. (a) M_2 garnet enclosing hercynite (Hc) and sillimanite coexists with corundum (Crn) in leucocratic gneiss. (b) M_4 cordierite (Crd) and hypidioblastic M_4 garnet (Grt_{M4}) grains around M_2 garnet porphyroblast (Grt_{M2}) in leucocratic gneiss. (c) Typical M_4 mineral assemblage that shows garnet, hercynite and sillimanite mantled by cordierite in leucocratic gneiss. (d) Inclusions of M_1 kyanite (Ky_{M1}) and staurolite (St) in M_2 garnet porphyroblast from a kyanite-bearing gneiss. (e) M_3 kyanite and staurolite replacing M_2 garnet in a kyanite-bearing gneiss. Both M_2 and M_3 minerals are mantled by M_4 cordierite. (f) M_3 kyanite (Ky_{M3}) and rutile (Rt) replacing M_2 garnet containing inclusions of M_1 kyanite (Ky_{M1}) in aluminous granulite. All photomicrographs taken under plane-polarized light.

matrix together with rutile and ilmenite. These M_3 minerals are often mantled by cordierite.

Kyanite–garnet gneiss

The kyanite–garnet gneiss occurs as discrete layers and isolated blocks in the diatexitic region. It consists primarily of garnet, biotite and kyanite, and contains variable amounts of sillimanite, plagioclase, quartz, cordierite and rare staurolite and hercynite. K-feldspar is absent in all the examined kyanite–garnet gneisses. These gneisses commonly preserve textural evidence for mineral growth at various metamorphic stages. M_1 kyanite, together with sillimanite, biotite and rare staurolite, occur as inclusions

within M_2 garnet porphyroblasts (Fig. 4d). On the other hand, texturally late M_3 kyanite occurs together with prismatic staurolite and rutile, replacing M_2 garnet porphyroblasts (Fig. 4e). Hercynite, pseudomorphic after staurolite, often coexists with M_3 kyanite and rutile in the matrix. In contrast to the leucocratic gneiss, kyanite is the dominant Al-silicate in the kyanite–garnet gneiss. Both M_2 and M_3 minerals are commonly mantled by M_4 cordierite (Fig. 4e), and are also locally replaced by M_5 andalusite in some kyanite–garnet gneisses.

Aluminous gneiss

The mineral assemblages of the aluminous gneisses are equivalent to those of garnet-enriched layers of the leucocratic gneiss, except for the rare occurrence of biotite. Both lithologies probably represent the residua after the extraction of significant amount of granitic melt, and could be complementary in composition to the widespread stock-like bodies of leucogranite. Kyanite is ubiquitous in aluminous gneisses, occurring not only as inclusions within M_2 garnet porphyroblasts but also as texturally later M_3 grains in the matrix. The latter commonly replace prismatic sillimanite, and, together with rutile, uncommonly overgrow biotite aggregates around resorbed M_2 garnet (Fig. 4f).

Mafic granulite

The majority of mafic granulites occur as boudinaged layers or isolated blocks within leucocratic gneisses and leucogranites. Mafic granulites also occur as remnants within amphibolites, and these metabasites apparently show the intrusion relationship with the host gneisses. M_2 mineral assemblages of the mafic granulite comprise orthopyroxene, plagioclase and quartz with or without clinopyroxene, garnet, hornblende and biotite. Garnet and clinopyroxene are exclusive to each other with rare exceptions. Primary M_2 hornblende is commonly present as discrete subhedral grains or minute inclusions within clinopyroxene of two-pyroxene granulites (Fig. 5a). Mafic granulites commonly show partial to complete retrogression to garnet amphibolites, where orthopyroxene and clinopyroxene are replaced by M_3 aggregates of cummingtonite and hornblende, respectively. Secondary M_3 garnet occurs as fine idioblastic crystals rimming pyroxene and plagioclase (Fig. 5b), but apparently does not mantle primary M_2 garnet. The retrogression probably occurred under static conditions, because primary textures are well preserved even in significantly retrogressed mafic granulites.

Together with typical mafic granulites described above, there is an orthopyroxene-free mafic gneiss (sample YK5H3), consisting of garnet, clinopyroxene, plagioclase and quartz. Primary M_2 garnet shows the overgrowth of secondary M_3 garnet at the outer rim, and clinopyroxene is replaced by green hornblende (Fig. 5c).

Amphibolites

Two types of amphibolites are distinguished on the basis of field occurrences and mineral parageneses. Type 1 amphibolites occur as sills or dykes that intrude leucocratic gneiss, and are commonly boudinaged. These amphibolites are pervasively intruded by pegmatitic veinlets stemming from the leucogranite, and are also rarely intruded by garnet-bearing leucogranite. Mineral assemblages consist primarily of hornblende and plagioclase, together with lesser amounts of garnet, cummingtonite and quartz. These assemblages are consistent with the M_3 assemblage of the mafic granulites. Some amphibolite bodies preserve remnants of mafic granulites, suggesting that type 1 amphibolites are the product of complete retrogression of mafic granulites.

Type 2 amphibolites occur as massive bodies, ranging up to a few tens of metres in width, and are not intruded by leucogranites or pegmatitic veins. These amphibolites consist primarily of garnet, hornblende and plagioclase together with minor quartz. In particular, they do not contain cummingtonite pseudomorphs after orthopyroxene. Thus, the protoliths of these massive amphibolites, similar in appearance to the MZGC amphibolite (Lee & Cho, 1995), are likely to have been emplaced after the granulite-facies metamorphism. Symplectites consisting of hornblende and plagioclase commonly mantle garnet porphyroblasts in both types of garnet amphibolite (Fig. 5d).

MINERAL CHEMISTRY

Minerals were analyzed using a JEOL 733 JXA electron microprobe at Seoul National University, with an operating voltage of 15 kV and a beam current of 10 nA. Beam diameter was typically 5 μm, but a wider beam of 20 μm was used for analyzing pyroxene and K-feldspar showing exsolution textures. Natural and synthetic oxides as well as silicate minerals were used as standards. Data acquisition and reduction were performed using an automated ZAF correction program. Representative analyses of minerals are given in Tables 2–8.

Garnet

M_2 garnet porphyroblasts from pelitic granulites are pyrope-rich almandines, containing minor amounts of grossular and spessartine components (Table 2; Fig. 6). Although original lithologies and bulk chemistries are

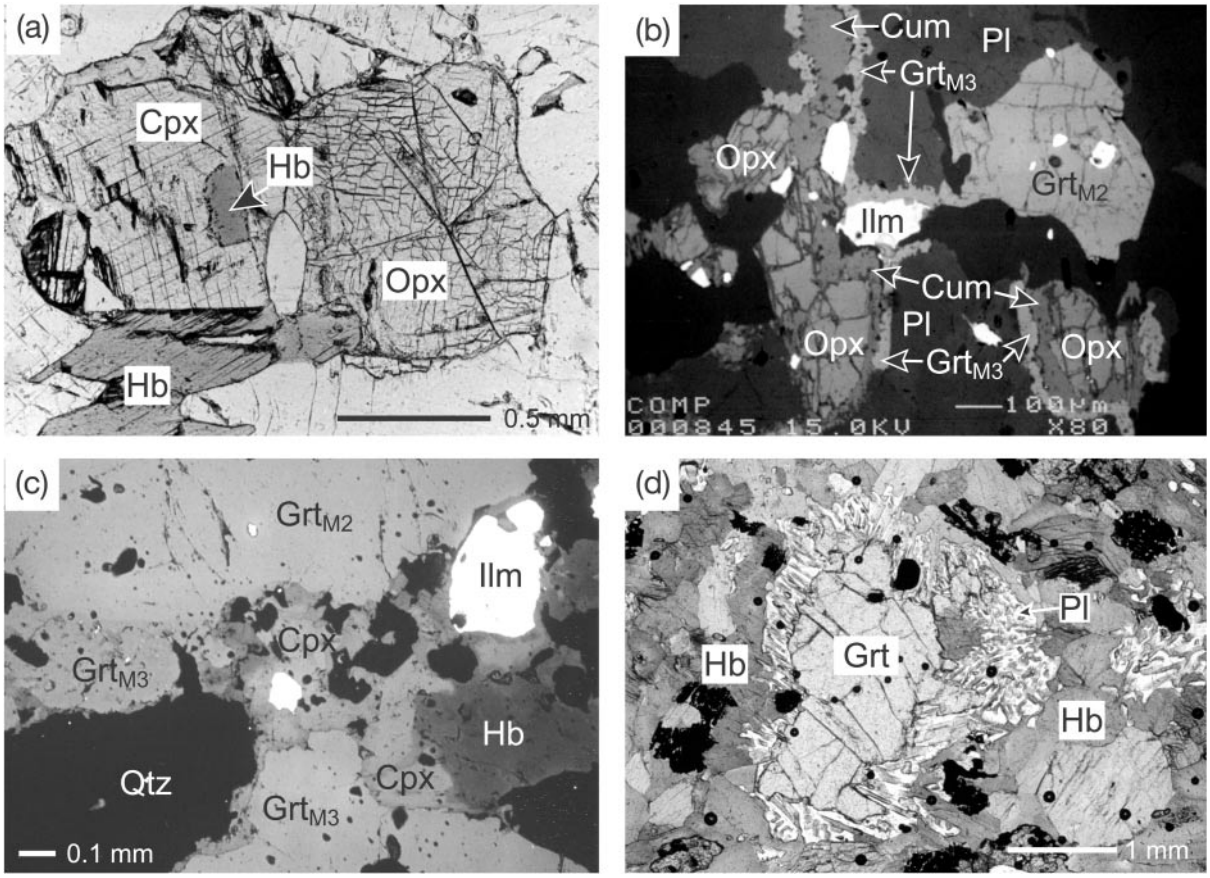

Fig. 5. Photomicrographs and BSE images showing various reaction textures in mafic granulites and amphibolites. (a) Coexistence of clinopyroxene (Cpx), orthopyroxene (Opx) and hornblende (Hb). (b) Retrogression of orthopyroxene to M_3 garnet (Grt_{M3}) and cummingtonite (Cum). It should be noted that M_3 garnet mantles orthopyroxene and its retrograde product of cummingtonite, but not M_2 garnet (Grt_{M2}). (c) Overgrowth of M_3 garnet around M_2 garnet porphyroblast. On the other hand, clinopyroxene is partially replaced by M_3 hornblende. (d) Hornblende–plagioclase (Pl) symplectite commonly observed in garnet amphibolites. All photomicrographs taken under plane-polarized light.

significantly affected by granulite-facies metamorphism and associated partial melting, garnet compositions are rather uniform for all types of pelitic granulites: 2–6 mol % for grossular, and 1–4 mol % for spessartine components, respectively. The Fe/(Fe + Mg) value of the garnet core ranges from 0·61 to 0·75, and is generally high in relatively small grains. Most M_2 garnet grains from pelitic granulites show a diffusional zoning pattern, characterized by increasing Fe/(Fe + Mg) and decreasing Mg towards the rim, and a slight enrichment of Mn at the outermost rim (Fig. 7a). This pattern is prominent especially in garnet grains that are corroded or mantled by other Fe–Mg minerals such as biotite and cordierite. In cordierite-bearing leucocratic gneisses, M_4 garnet is similar in grossular (3–8 mol %) and spessartine (1–2 mol %) contents to M_2 garnet, but significantly higher in the almandine content (74–79 mol %) (Fig. 6). In addition, the Fe/(Fe + Mg) value ranges from 0·74 to 0·82, and is generally similar to that of the rim of M_2 garnet.

In mafic granulites, M_2 garnet is more enriched in the grossular component than that in the pelitic granulites (Fig. 6). The almandine contents (66–71 mol %) are rather constant, but the grossular contents (6–18 mol %), generally complementary to pyrope contents, are variable. The Fe/(Fe + Mg) value ranges from 0·75 to 0·79, and compositional zoning is not prominent, in contrast to M_2 garnet from the pelitic granulites. M_3 garnet mainly occurs as coronas around pyroxene, and its grossular content ranges from 11 to 27 mol %. The compositional variations of M_2 and M_3 garnets are shown in Fig. 7b. The Fe/(Fe + Mg) value is more or less constant throughout the whole grain of garnet, but the grossular content increases abruptly in the M_3 garnet.

Biotite

Biotite is one of the major constituents in pelitic granulites, and has apparently formed at various metamorphic

Table 2: Representative analyses of garnet

	Pelitic rocks							Mafic rocks					
Sample no.:	HC22-1		HC85D			YK101D		HC-85E		HC14-1		YK5H-3	
	M_2c	M_2r	M_2c	M_2r	M_4	M_2c	M_2r	M_2c	M_2r	M_2	M_3	M_2	M_3
SiO_2	38·55	38·05	38·62	37·75	37·89	38·39	37·42	38·30	37·72	38·11	37·87	37·07	37·42
Al_2O_3	21·85	21·57	21·72	21·44	21·62	21·60	21·20	21·72	21·39	21·54	21·54	21·15	21·45
FeO*	28·68	32·27	31·10	32·70	33·23	30·79	34·66	31·52	31·48	29·94	27·13	31·12	27·32
MgO	9·04	6·18	7·30	6·01	6·03	8·14	4·77	5·65	5·52	5·75	4·54	1·59	1·19
MnO	0·56	0·68	0·33	0·35	0·49	0·33	0·55	0·64	0·61	1·08	0·65	0·49	0·33
CaO	0·97	0·99	0·96	0·98	0·93	0·99	0·97	2·60	2·49	2·74	7·59	8·02	11·76
Total	99·64	99·74	100·03	99·22	100·17	100·23	99·58	100·43	99·21	99·15	99·31	99·44	99·47
Cations per 12 oxygens													
Si	2·99	3·00	3·01	3·00	2·98	2·99	2·99	3·00	3·00	3·01	2·99	2·99	2·99
Al	2·00	2·01	2·00	2·01	2·01	1·98	2·00	2·01	2·01	2·01	2·01	2·01	2·02
Fe^{2+}	1·86	2·13	2·03	2·17	2·19	2·00	2·32	2·07	2·09	1·98	1·79	2·10	1·82
Mg	1·05	0·73	0·85	0·71	0·71	0·94	0·57	0·66	0·65	0·68	0·53	0·19	0·14
Mn	0·04	0·05	0·02	0·02	0·03	0·02	0·04	0·04	0·04	0·07	0·04	0·03	0·02
Ca	0·08	0·08	0·08	0·08	0·08	0·08	0·08	0·22	0·21	0·23	0·64	0·69	1·01
Total	8·01	7·99	7·99	8·00	8·00	8·02	8·00	7·99	8·00	7·98	8·01	8·01	8·00
Fe/(Fe + Mg)	0·64	0·75	0·70	0·75	0·76	0·68	0·80	0·76	0·76	0·74	0·77	0·92	0·93
Alm	0·62	0·71	0·68	0·73	0·73	0·66	0·77	0·69	0·70	0·67	0·59	0·70	0·61
Prp	0·35	0·24	0·28	0·24	0·24	0·31	0·19	0·22	0·22	0·23	0·18	0·06	0·05
Sps	0·01	0·02	0·01	0·01	0·01	0·01	0·01	0·01	0·01	0·02	0·01	0·01	0·01
Grs	0·03	0·03	0·03	0·03	0·03	0·03	0·03	0·07	0·07	0·08	0·21	0·23	0·34

*Total Fe as FeO.
c, core; r, rim; Alm = Fe/M, Prp = Mg/M, Sps = Mn/M and Grs = Ca/M, where M = (Fe + Mg + Mn + Ca).

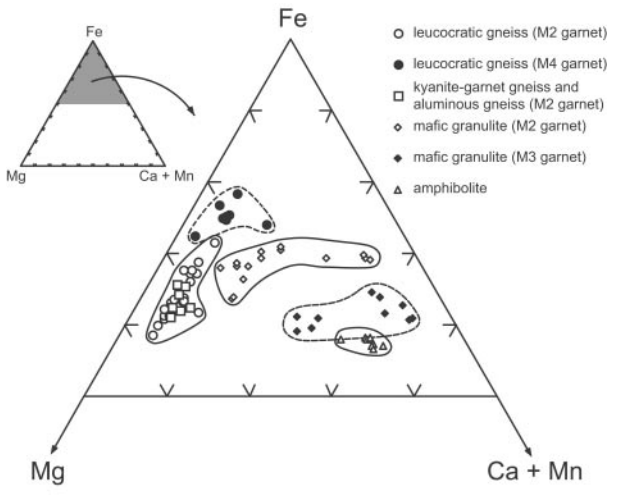

Fig. 6. Fe–Mg–(Ca + Mn) diagram showing the compositions of garnet analyzed from various rock types.

stages. Biotite commonly coexists with Ti-oxide phases such as ilmenite and rutile. Primary M_2 biotite, mainly occurring as the matrix phase, is generally higher in Ti content (0·32–0·55 atoms per formula unit, a.p.f.u.) than secondary M_3 biotite (0·14–0·28 a.p.f.u.). Primary biotite is well preserved, especially in the cordierite-bearing leucocratic gneiss, and its Fe/(Fe + Mg) value varies from 0·25 to 0·55. In the cordierite-absent leucocratic gneiss, however, the composition of the Ti-rich, primary biotite is enriched in Mg. Biotite, occurring as inclusions in M_2 phases such as garnet and K-feldspar, shows a similar composition to the Ti-rich, magnesian biotite (Table 3). The primary biotite is generally absent in kyanite–garnet and aluminous gneisses. The Cl and F contents of primary biotite are minor (<0·02 a.p.f.u.), except for one sample, HY7, where the Cl content reaches 0·29–0·37 a.p.f.u. (Table 3).

Secondary biotite occurs mainly as a part of the late-stage assemblages that replaces M_2 minerals, and shows higher Fe/(Fe + Mg) and lower Ti content than primary biotite (Table 3). This biotite is common mainly in

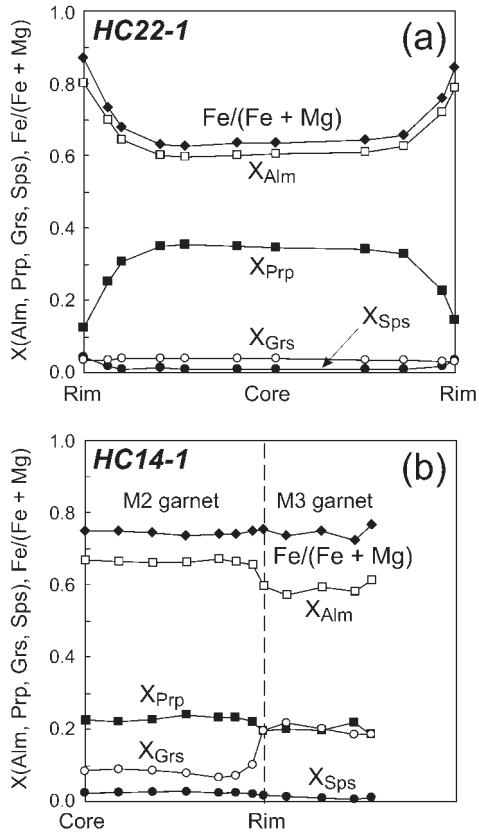

Fig. 7. Garnet zoning profiles from (a) pelitic granulite (HC22-1) and (b) mafic granulite (HC14-1). The length of each profile is approximately 1·0 and 0·8 mm, respectively. Traverse (b) shows the significant compositional change across the boundary between M_2 and M_3 garnets.

kyanite–garnet and aluminous gneisses, and rare in cordierite-absent leucocratic gneiss.

Primary M_2 biotite is rare in mafic granulites, but often coexists with M_2 hornblende in two-pyroxene granulites. However, post-M_2 biotite is ubiquitous in the retrogressed mafic granulite. The Fe/(Fe + Mg) value of M_2 biotite (0·40–0·41) is generally lower than that of post-M_2 biotite (0·41–0·47). The F content (0·27–0·49 a.p.f.u.) of biotite from mafic granulites appears to be higher than that from pelitic granulites (Table 3).

Pyroxenes

Pyroxenes are major constituents of the mafic granulite, but are absent in the pelitic granulite. Most orthopyroxene grains are ferro-hypersthene, and less commonly hypersthene with Fe/(Fe + Mg) values of 0·48–0·67. The Al contents of orthopyroxene vary from 0·02 to 0·15 a.p.f.u. in clinopyroxene-bearing granulite, and from 0·04 to 0·13 in garnet-bearing granulites (Table 4). Some grains are zoned towards low Al at the rim, and the difference in Al contents between core and rim reaches ~0·015 a.p.f.u. (Table 4). The variation in Fe and Mg contents is negligible, but Fe/(Fe + Mg) generally decreases towards the rim.

The clinopyroxene is augite with Fe/(Fe + Mg) values ranging from 0·40 to 0·66. The Al content varies from 0·06 to 0·08 a.p.f.u. in two-pyroxene granulites, but is <0·04 a.p.f.u. for clinopyroxene coexisting with garnet (Table 4). In the latter case, clinopyroxene is slightly zoned in Al with core-to-rim variations of ~0·01 a.p.f.u.

Amphibole

Primary M_2 amphiboles in two-pyroxene granulites are mostly magnesio-hornblende, and rarely edenitic and ferro-tschermakitic hornblende (Leake, 1978). The Si content ranges from 6·26 to 7·17 a.p.f.u. and $(Na + K)^A$ from 0·11 to 0·53 a.p.f.u. The Fe/(Fe + Mg) value varies between 0·30 and 0·65, and the Ti content ranges from 0·07 to 0·14 a.p.f.u. (Table 5). The Cl content (0·14–0·31 a.p.f.u.) of M_2 hornblende is higher than the F content (<0·02 a.p.f.u.).

M_3 amphiboles from the mafic granulite can be divided into calcic and iron–magnesium–manganese groups, respectively. The majority of calcic amphiboles are magnesio-hornblende, with Si of 6·59–6·71 a.p.f.u. and $(Na + K)^A$ of 0·12 to 0·18. The Fe/(Fe + Mg) value ranges from 0·32 to 0·35 and the Ti content from 0·05 to 0·08 a.p.f.u. In the garnet–clinopyroxene-bearing mafic granulites, however, the calcic amphiboles are higher in Fe/(Fe + Mg) (0·72–0·85) and $(Na + K)^A$ (0·69–0·80 a.p.f.u.). These amphiboles are ferro-pargasite with Si contents of 6·13–6·54 a.p.f.u. All the M_3 calcic amphiboles are lower in Ti content than M_2 amphiboles. Iron–magnesium–manganese amphiboles are cummingtonite with Si of 7·65–7·91 a.p.f.u. and Fe/(Fe + Mg) value of 0·43–0·47 (Table 5). The F content of cummingtonite (<0·11 a.p.f.u.) appears to be higher than that of M_2 hornblende.

In the amphibolites, all the analyzed amphiboles are tschermakitic and magnesio-hornblende with Si of 6·33–6·69 a.p.f.u. and $(Na + K)^A$ of 0·20–0·39 a.p.f.u. The Fe/(Fe + Mg) value varies between 0·37 and 0·48, and the Ti content between 0·04 and 0·14 a.p.f.u.

Cordierite

The Fe/(Fe + Mg) value of cordierite ranges from 0·29 to 0·34 in leucocratic gneisses, and from 0·26 to 0·38 in kyanite–garnet gneisses. The channel cations consisting of Na and K in cordierite are generally higher in the leucocratic gneiss (0·02–0·09 a.p.f.u.) than in the kyanite–garnet gneiss (0·01–0·03 a.p.f.u.) (Table 6). Some cordierites are zoned with decreasing Fe/(Fe + Mg) toward

Table 3: Representative analyses of biotite

	Pelitic rocks							Mafic rocks		
Sample no.:	HC19-1	HC22-2		HC85D		HY7	HC83B	HC81A		HC85E
	p	p	s	p	i(Grt)	p	p	p	s	p
SiO_2	34·54	37·30	36·28	36·17	36·63	34·76	36·10	37·30	37·51	36·72
TiO_2	3·65	3·76	1·90	4·69	4·13	3·52	4·84	2·23	1·60	3·13
Al_2O_3	18·35	16·72	17·98	17·79	17·75	18·57	18·01	15·70	16·21	15·02
FeO*	18·97	14·25	14·43	16·23	13·31	19·63	14·26	16·63	16·60	16·07
MgO	9·32	14·04	13·34	11·55	12·83	9·02	12·81	13·41	14·49	13·17
MnO	0·06	0·00	0·06	0·00	0·00	0·00	0·00	0·07	0·06	0·00
CaO	0·01	0·00	0·00	0·01	0·00	0·00	0·00	0·00	0·05	0·00
Na_2O	0·17	0·29	0·17	0·14	0·21	0·13	0·17	0·49	0·29	0·22
K_2O	10·56	10·04	10·00	9·97	9·74	11·08	11·24	9·45	8·69	8·97
F	0·01	0·01	n.d.	0·00	n.d.	0·01	0·02	0·80	0·98	n.d.
Cl	0·22	0·04	n.d.	0·03	n.d.	1·12	0·08	n.d.	n.d.	n.d.
H_2O†	2·45	2·84	3·03	2·59	2·50	2·16	2·38	2·80	3·29	3·09
O = F, Cl	−0·05	−0·01	0·00	−0·01	0·00	−0·26	−0·03	−0·33	−0·41	0·00
Total	98·30	99·29	97·20	99·15	97·09	100·01	99·90	98·88	99·77	96·40
Cations per 24(O, OH, F, Cl)										
Si	5·45	5·63	5·59	5·54	5·64	5·46	5·49	5·71	5·63	5·72
Ti	0·43	0·43	0·22	0·54	0·48	0·42	0·55	0·26	0·18	0·37
Al	3·42	2·98	3·27	3·21	3·22	3·44	3·23	2·84	2·87	2·76
Fe^{2+}	2·50	1·80	1·86	2·08	1·71	2·58	1·81	2·13	2·08	2·09
Mg	2·19	3·16	3·06	2·63	2·94	2·11	2·90	3·06	3·24	3·06
Mn	0·01	0·00	0·01	0·00	0·00	0·00	0·00	0·01	0·01	0·00
Ca	0·00	0·00	0·00	0·00	0·00	0·00	0·00	0·00	0·01	0·00
Na	0·05	0·08	0·05	0·04	0·06	0·04	0·05	0·14	0·08	0·07
K	2·13	1·93	1·96	1·95	1·91	2·22	2·18	1·84	1·66	1·78
Total	16·18	16·02	16·01	15·99	15·97	16·26	16·23	15·99	15·75	15·85
F	0·00	0·00	n.d.	0·00	n.d.	0·01	0·01	0·38	0·46	n.d.
Cl	0·06	0·01	n.d.	0·01	n.d.	0·29	0·02	n.d.	n.d.	n.d.
OH	2·58	2·87	3·11	2·64	2·56	2·26	2·41	2·86	3·29	3·22
Fe/(Fe + Mg)	0·53	0·36	0·38	0·44	0·37	0·55	0·38	0·41	0·39	0·41

*Total Fe as FeO.
†H content calculated from charge-balance constraint, assuming that the occupancy of the OH site is four.
p, primary; s, secondary; i, inclusion enclosed in mineral within parenthesis; n.d., not determined.

rims, and the difference between core and rim reaches ~0·09.

Feldspars

The compositional ranges of plagioclase are distinctly different between pelitic (~$An_{30–50}$) and mafic (~$An_{50–90}$) rocks, as can be inferred from the difference in their bulk chemistries (Table 7). In pelitic granulites, most plagioclase grains are andesine, and their orthoclase contents are low (0–3 mol %). The orthoclase component in some plagioclase grains exsolved from K-feldspar hosts in aluminous gneiss ranges up to ~17 mol %. Plagioclase commonly shows asymmetric reverse zoning with increasing anorthite content toward the rim, particularly when it is in contact with garnet porphyroblasts.

In two-pyroxene mafic granulites, most plagioclase grains are anorthite-rich ($An_{76–92}$). Plagioclase compositions in the garnet-bearing mafic granulite vary significantly even within individual specimens, and are

Table 4: Representative analyses of pyroxene

Sample no.:	HC84A		HC85G		HC85A		HC85E	HC87	YK5D2	YK5H	
	Cpx av.[1]	Opx av.[1]	Cpx av.[1]	Opx av.[1]	Opx c	Opx r	Opx	Opx	Opx	Cpx c	Cpx r
SiO_2	51·06	50·64	50·01	49·06	49·85	50·17	50·37	50·36	49·45	50·30	50·54
TiO_2	0·25	0·12	0·26	0·17	0·14	0·13	0·12	0·12	0·13	0·12	0·14
Al_2O_3	1·56	0·70	1·35	0·81	3·28	2·95	1·89	1·64	2·68	0·92	0·85
FeO*	13·38	30·31	18·17	37·46	28·80	28·76	31·71	31·71	31·18	16·48	16·76
MgO	11·33	15·82	8·24	10·91	16·81	17·42	15·16	14·66	15·40	8·29	8·20
MnO	0·32	0·60	0·27	0·49	0·16	0·17	0·25	0·27	0·27	0·04	0·07
CaO	21·27	0·93	21·04	1·24	0·21	0·13	0·19	0·47	0·22	23·18	22·95
Na_2O	0·18	0·01	0·22	0·00	0·03	0·01	0·02	0·03	0·00	0·11	0·12
K_2O	0·01	0·01	0·00	0·01	0·01	0·01	0·00	0·00	0·01	0·00	0·01
Total	99·65	99·49	99·57	100·14	99·29	99·74	99·69	99·24	99·34	99·44	99·62
Cations per 6 oxygens											
Si	1·96	1·98	1·96	1·97	1·93	1·93	1·97	1·98	1·93	1·97	1·97
Ti	0·01	0·00	0·01	0·01	0·00	0·00	0·00	0·00	0·00	0·00	0·00
Al	0·07	0·03	0·06	0·04	0·15	0·13	0·09	0·08	0·12	0·04	0·04
Fe^{2+}	0·43	0·99	0·59	1·26	0·93	0·92	1·03	1·04	1·02	0·54	0·55
Mg	0·65	0·92	0·48	0·65	0·97	1·00	0·88	0·86	0·90	0·48	0·48
Mn	0·01	0·02	0·01	0·02	0·01	0·01	0·01	0·01	0·01	0·00	0·00
Ca	0·87	0·04	0·88	0·05	0·01	0·01	0·01	0·02	0·01	0·97	0·96
Na	0·01	0·00	0·02	0·00	0·00	0·00	0·00	0·00	0·00	0·01	0·01
K	0·00	0·00	0·00	0·00	0·00	0·00	0·00	0·00	0·00	0·00	0·00
Total	4·01	4·00	4·01	4·00	4·00	4·00	3·99	3·98	4·00	4·01	4·01
Fe/(Fe + Mg)	0·40	0·52	0·55	0·66	0·49	0·48	0·54	0·55	0·53	0·53	0·53

*Total Fe as FeO.
[1]Average of 6–15 analyses using 20 μm wide beam.
Abbreviations as in Tables 2 and 3.

$An_{46–58}$ and $An_{68–79}$, suggesting a compositional gap between An_{58} and An_{68}. Reverse zoning of plagioclase is common in mafic granulites, but often shows irregular patterns.

In garnet-bearing amphibolites, plagioclase is andesine ($An_{38–48}$). Most grains of plagioclase show asymmetric normal zoning, in contrast to mafic granulites.

Except for kyanite–garnet gneisses, perthitic K-feldspar is ubiquitous in all the pelitic granulites. Its orthoclase content ranges from 55 to 87 mol %, and the anorthite content from 0 to 5 mol % (Table 7). K-feldspar is absent in most mafic granulites, but rarely observed as discontinuous or patchy lamellae within the exsolved antiperthite.

Spinel

The spinel in all pelitic granulites belongs to the gahnite–hercynite–spinel solid solution, and its Fe/(Fe + Mg) value varies widely (0·60–0·90; Table 8; Fig. 8). The chromite content is generally low in most spinels, but rarely reaches 0·12 mol % in some cordierite-bearing leucocratic gneisses. Low values of Fe/(Fe + Mg) are recorded in spinel occurring as inclusions in M_2 garnet, and vary from 0·60 to 0·76. In these spinel inclusions, the Zn content ranges from 0·06 to 0·08 a.p.f.u. On the other hand, M_3 spinel grains in the kyanite–garnet gneiss range in Fe/(Fe + Mg) from 0·85 to 0·90, and in the Zn content from 0·14 to 0·18 a.p.f.u. In the cordierite-bearing leucocratic gneisses, Fe/(Fe + Mg) of M_4 spinel varies from 0·71 to 0·85, and the Zn content is 0·06–0·29 a.p.f.u.

Staurolite

Staurolite occurs as either inclusions within M_2 garnet or retrograde grains replacing this garnet. Both types of

Table 5: Representative analyses of amphibole

Sample no.:	HC84A		HC85G		HC85A	HC81A	HC14-1		YK5K	HC130
	Hb	Hb	Hb	Hb	Cum	Cum	Hb	Cum	Hb	Hb
	M_2	M_2	M_2	M_2	M_3	M_3	M_3	M_3	M_3	M_4
SiO_2	44·66	45·26	39·99	39·05	52·28	52·38	45·19	52·96	38·54	43·27
TiO_2	1·06	1·02	1·53	2·34	0·07	0·06	0·63	0·13	0·87	0·97
Al_2O_3	9·69	9·94	12·44	12·51	3·37	1·95	10·95	1·59	13·18	12·92
Fe_2O_3*	3·59	2·88	2·20	1·10	1·84	2·13	8·08	0·84	3·35	4·11
FeO*	12·31	13·23	19·72	20·98	22·70	23·72	9·51	23·64	24·90	12·42
MgO	11·29	10·80	6·25	5·40	16·73	15·92	11·03	16·27	2·45	9·52
MnO	0·13	0·11	0·08	0·09	0·08	0·47	0·11	0·22	0·05	0·22
CaO	11·57	11·33	11·32	10·85	0·20	0·50	11·27	1·27	11·62	11·43
Na_2O	1·08	1·17	1·25	1·36	0·34	0·30	1·04	0·19	1·47	1·25
K_2O	1·28	1·27	2·29	2·47	0·01	0·00	0·52	0·00	1·25	0·58
F	0·00	0·02	0·00	0·01	0·13	0·23	n.d.	n.d.	n.d.	n.d.
Cl	0·65	0·70	0·98	1·07	n.d.	n.d.	n.d.	n.d.	n.d.	n.d.
H_2O†	1·83	1·82	1·67	1·61	1·98	1·92	2·05	2·03	1·88	2·01
O = F, Cl	−0·15	−0·16	−0·22	−0·25	−0·06	−0·10	0·00	0·00	0·00	0·00
Total	99·14	99·53	99·73	98·84	99·73	99·58	100·39	99·14	99·57	98·71
Cations per 24 (O, OH, F, Cl)										
Si	6·69	6·75	6·24	6·19	7·65	7·75	6·59	7·83	6·13	6·46
Ti	0·12	0·11	0·18	0·28	0·01	0·01	0·07	0·01	0·10	0·11
Al	1·71	1·75	2·29	2·34	0·58	0·34	1·88	0·28	2·47	2·28
Fe^{3+}*	0·40	0·32	0·26	0·13	0·20	0·24	0·89	0·09	0·40	0·46
Fe^{2+}	1·95	1·97	2·83	2·91	2·98	3·17	2·05	3·02	3·71	2·01
Mg	2·52	2·40	1·45	1·27	3·65	3·51	2·40	3·58	0·58	2·12
Mn	0·02	0·01	0·01	0·01	0·01	0·06	0·01	0·03	0·01	0·03
Ca	1·86	1·81	1·89	1·84	0·03	0·08	1·76	0·20	1·98	1·83
Na	0·31	0·34	0·38	0·42	0·10	0·09	0·29	0·05	0·45	0·36
K	0·25	0·24	0·46	0·50	0·00	0·00	0·10	0·00	0·25	0·11
Total	15·82	15·71	15·98	15·89	15·20	15·24	16·04	15·09	16·09	15·76
F	0·00	0·01	0·00	0·01	0·06	0·11	n.d.	n.d.	n.d.	n.d.
Cl	0·17	0·18	0·26	0·29	n.d.	n.d.	n.d.	n.d.	n.d.	n.d.
OH†	1·83	1·81	1·74	1·70	1·94	1·89	2·00	2·00	2·00	2·00
Fe/(Fe + Mg)	0·44	0·45	0·66	0·70	0·45	0·47	0·46	0·46	0·86	0·49

*Fe^{2+} and Fe^{3+} calculated on the basis of 13 cations excluding Ca, Na and K for hornblende, and 15 cations excluding Na and K for cummingtonite.
†H content calculated from charge-balance constraint, assuming that the occupancy of the OH site is two.
Abbreviations as in Tables 2 and 3.

staurolite are similar in composition. The Fe/(Fe + Mg) value ranges from 0·70 to 0·72, and the Zn content from 0·22 to 0·37 a.p.f.u. (Table 8; Fig. 8).

Fe–Ti oxide

Ilmenite is the dominant Fe–Ti oxide in both pelitic and mafic granulites, and has <4 mol % hematite component (Table 8). Rutile occurs as a discrete grain or intergrows with ilmenite especially in kyanite-bearing rocks. Magnetite and hematite are absent in all types of granulites.

THE FIVE METAMORPHIC STAGES AND THEIR PHYSICAL CONDITIONS

Five metamorphic stages (M_1–M_5) were deduced on the basis of inclusion-mineral relationships, reaction textures, and the P–T stability of minerals in the different lithologies

Table 6: Representative analyses of cordierite

Sample no.:	HC83B	HC85B		HC85D	YK19	HC130C		YK51B	YK51C2	
		c	r			c	r		c	r
SiO_2	48·75	48·94	48·56	48·60	48·69	48·33	48·43	48·56	48·23	48·82
TiO_2	0·00	0·00	0·00	0·00	0·00	0·00	0·00	0·00	0·03	0·00
Al_2O_3	32·78	33·46	33·41	33·12	33·04	33·16	33·16	33·51	33·21	33·07
FeO*	7·84	6·74	6·40	7·75	6·63	7·77	7·92	7·56	7·82	5·62
MgO	8·43	8·75	8·64	8·44	9·02	7·88	8·21	8·10	8·32	9·37
MnO	0·00	0·01	0·02	0·00	0·00	0·14	0·15	0·11	0·02	0·00
CaO	0·00	0·04	0·00	0·00	0·00	0·00	0·00	0·00	0·06	0·00
Na_2O	0·12	0·14	0·16	0·12	0·03	0·05	0·02	0·09	0·07	0·14
K_2O	0·00	0·02	0·00	0·01	0·00	0·02	0·01	0·00	0·01	0·00
Total	97·93	98·09	97·20	98·04	97·41	97·34	97·90	97·94	97·78	97·00
Cations per 18 oxygens										
Si	5·02	5·01	5·01	5·00	5·01	5·01	5·00	5·00	4·98	5·02
Ti	0·00	0·00	0·00	0·00	0·00	0·00	0·00	0·00	0·00	0·00
Al	3·98	4·03	4·06	4·02	4·01	4·05	4·03	4·06	4·04	4·01
Fe^{2+}	0·68	0·58	0·55	0·67	0·57	0·67	0·68	0·65	0·68	0·48
Mg	1·29	1·33	1·33	1·30	1·38	1·22	1·26	1·24	1·28	1·44
Mn	0·00	0·00	0·00	0·00	0·00	0·01	0·01	0·01	0·00	0·00
Ca	0·00	0·00	0·00	0·00	0·00	0·00	0·00	0·00	0·01	0·00
Na	0·02	0·03	0·03	0·02	0·01	0·01	0·00	0·02	0·01	0·03
K	0·00	0·00	0·00	0·00	0·00	0·00	0·00	0·00	0·00	0·00
Total	11·00	10·99	10·98	11·00	10·98	10·97	10·99	10·98	11·00	10·98
Fe/(Fe + Mg)	0·34	0·30	0·29	0·34	0·29	0·36	0·35	0·34	0·35	0·25

*Total Fe as FeO.
Abbreviations as in Table 2.

(Table 1). In this section we describe various reactions responsible for producing mineral assemblages at each metamorphic stage, and *P–T* conditions estimated from various geothermobarometers. These results are used to construct a composite *P–T* path, consisting of two distinct clockwise *P–T* trajectories whose temporal relationships are given in the next section.

M_1 metamorphism

Prograde metamorphism occurred at medium to high pressures, as inferred from the inclusions of kyanite and rare staurolite in M_2 garnet of kyanite–garnet and aluminous gneisses. These inclusions are absent in the leucocratic gneiss, where zincian hercynite occurs as inclusions within M_2 garnet. This observation may indicate the former presence of staurolite, because hercynite is commonly produced by the breakdown of staurolite in high-grade rocks (Stoddard, 1979; Cesare, 1994). Although quantitative *P–T* conditions could not be obtained because of the lack of appropriate mineral pairs for geothermobarometry, all of the above observations indicate that prograde metamorphism was initiated within the kyanite stability field.

M_2 metamorphism

The M_2 stage, corresponding to peak granulite-facies metamorphism, is manifested by the occurrence of orthopyroxene in mafic granulites. Moreover, the lack of garnet–clinopyroxene–orthopyroxene assemblage indicates medium-pressure conditions for granulite-facies metamorphism (Green & Ringwood, 1967).

The *P–T* conditions of M_2 were estimated using the two-pyroxene geothermometer and garnet–orthopyroxene–plagioclase–quartz geothermobarometer for mafic granulites. Except for the two-pyroxene geothermometer, the *P–T* conditions were calculated using the core–core pairs of minerals, based on the assumption

Table 7: Representative analyses of feldspar

	Pelitic rocks									Mafic rocks			
Sample no.:	HC22-1			HC85D			YK51C2		YK101D	HC84B	HC85E		HC130
	Pl(c)	Pl(r)	Ksp(av.)*	Pl(c)	Pl(r)	Ksp(av.)*	Pl(c)	Pl(r)	Ksp(av.)*	Pl	Pl(c)	Pl(r)	Pl
SiO_2	59·76	59·20	63·72	60·61	61·18	64·41	59·01	59·37	64·82	46·07	55·68	54·32	56·93
Al_2O_3	25·13	25·34	18·99	24·35	24·68	18·96	25·85	25·46	18·91	35·12	28·62	29·09	26·61
CaO	6·49	6·97	0·43	5·69	6·19	0·41	7·15	7·39	0·67	17·54	10·32	10·86	9·44
Na_2O	7·72	7·72	1·55	8·35	8·44	2·47	8·06	7·72	3·62	1·56	5·98	5·58	5·98
K_2O	0·35	0·28	14·60	0·14	0·16	13·54	0·11	0·05	10·88	0·03	0·11	0·07	0·08
Total	99·45	99·50	99·28	99·14	100·64	99·79	100·18	99·99	98·91	100·32	100·72	99·91	99·05
Cations per 8 oxygens													
Si	2·68	2·66	2·96	2·72	2·71	2·96	2·63	2·65	2·97	2·11	2·49	2·45	2·57
Al	1·33	1·34	1·04	1·29	1·29	1·03	1·36	1·34	1·02	1·90	1·51	1·55	1·42
Ca	0·31	0·33	0·02	0·27	0·29	0·02	0·34	0·35	0·03	0·86	0·49	0·52	0·46
Na	0·67	0·67	0·14	0·73	0·72	0·22	0·70	0·67	0·32	0·14	0·52	0·49	0·52
K	0·02	0·02	0·86	0·01	0·01	0·79	0·01	0·00	0·64	0·00	0·01	0·00	0·00
Total	5·01	5·02	5·02	5·01	5·02	5·03	5·04	5·02	4·99	5·01	5·01	5·01	4·97
An	0·31	0·33	0·02	0·27	0·29	0·02	0·33	0·34	0·03	0·86	0·49	0·52	0·46
Ab	0·67	0·66	0·14	0·72	0·71	0·21	0·67	0·65	0·32	0·14	0·51	0·48	0·53
Or	0·02	0·02	0·84	0·01	0·01	0·77	0·01	0·00	0·64	0·00	0·01	0·00	0·00

*Average of 10–20 analyses using 20 μm wide beam.
An = Ca/M, Ab = Na/M and Or = K/M, where M = (Ca + Na + K). Abbreviations as in Table 2.

Table 8: Representative analyses of spinel, staurolite and ilmenite

	Spinel					Staurolite		Ilmenite						
								Pelitic rocks			Mafic rocks			
Sample no.:	HC22-1	HC79-6	HC83B	HC85B	YK51C	HC130C	YK51C	HC22-1	HC83B	HY18	HC84B	HC85A	YK5D2	YK5H3
	M_1	M_1	M_4	M_4	M_3	M_3	M_3							
SiO_2	0·00	0·11	0·00	0·07	0·01	27·96	26·68	0·06	0·01	0·03	0·00	0·00	0·05	0·01
TiO_2	0·03	0·00	0·09	0·00	0·14	0·35	0·89	52·1	50·88	50·35	51·38	50·57	51·35	51·07
Al_2O_3	60·05	62·01	58·33	55·70	53·83	52·74	53·35	0·01	0·02	0·03	0·00	0·03	0·02	0·01
FeO*	26·27	25·43	22·51	29·59	29·38	12·76	12·97	46·53	46·16	47·53	46·87	47·10	45·32	46·93
MgO	6·12	9·17	4·32	3·10	2·66	1·67	1·57	0·29	0·28	0·21	0·07	0·00	0·43	0·14
MnO	0·04	0·03	0·11	0·18	0·16	0·10	0·04	0·33	0·34	0·13	0·79	0·63	0·18	0·24
CaO	0·00	0·00	0·07	0·03	0·04	0·00	0·01	0·05	0·07	0·04	0·04	0·07	0·04	0·00
Na_2O	0·22	0·05	0·38	0·13	0·28	0·02	0·03	0·02	0·05	0·00	0·02	0·00	0·00	0·00
K_2O	0·01	0·00	0·02	0·00	0·04	0·00	0·00	0·03	0·06	0·01	0·05	0·02	0·01	0·04
Cr_2O_3	1·69	0·93	n.d.	5·18	4·33	0·23	n.d.	n.d.	n.d.	n.d.	0·08	0·21	0·25	0·294
ZnO	5·09	3·13	13·77	5·37	7·76	1·58	1·79	n.d.	n.d.	n.d.	0·34	0·29	n.d.	n.d.
Total	99·52	100·86	99·60	99·35	98·63	97·41	97·33	99·42	97·87	98·33	99·64	98·92	97·65	98·72
Cations per 4, 46 and 3 oxygens for spinel, staurolite and ilmenite, respectively														
Si	0·00	0·00	0·00	0·00	0·00	7·82	7·50	0·00	0·00	0·00	0·00	0·00	0·00	0·00
Ti	0·00	0·00	0·00	0·00	0·00	0·07	0·19	0·99	0·98	0·97	0·98	0·97	1·00	0·98
Al	1·98	1·97	1·98	1·90	1·88	17·40	17·69	0·00	0·00	0·00	0·00	0·00	0·00	0·00
Fe^{2+}	0·61	0·57	0·54	0·72	0·73	2·98	3·05	0·99	0·99	1·02	0·99	1·00	0·98	1·00
Mg	0·25	0·37	0·19	0·13	0·12	0·70	0·66	0·01	0·01	0·01	0·00	0·00	0·02	0·01
Mn	0·00	0·00	0·00	0·00	0·00	0·02	0·01	0·01	0·01	0·00	0·02	0·01	0·00	0·01
Ca	0·00	0·00	0·00	0·00	0·00	0·00	0·00	0·00	0·00	0·00	0·00	0·00	0·00	0·00
Na	0·01	0·00	0·02	0·01	0·02	0·01	0·02	0·00	0·00	0·00	0·00	0·00	0·00	0·00
K	0·00	0·00	0·00	0·00	0·00	0·00	0·96	0·00	0·00	0·00	0·00	0·00	0·00	0·00
Cr	0·04	0·02	n.d.	0·12	0·10	0·05	n.d.	n.d.	n.d.	n.d.	0·00	0·00	0·01	0·01
Zn	0·11	0·06	0·29	0·11	0·17	0·33	0·37	n.d.	n.d.	n.d.	0·01	0·01	n.d	n.d.
Total	3·00	3·00	3·02	2·99	3·02	29·38	30·44	2·00	2·00	2·00	2·00	2·00	2·00	2·00
Fe/(Fe + Mg)	0·71	0·61	0·74	0·84	0·86	0·81	0·82							

*Total Fe as FeO.
Abbreviations as in Tables 2 and 3.

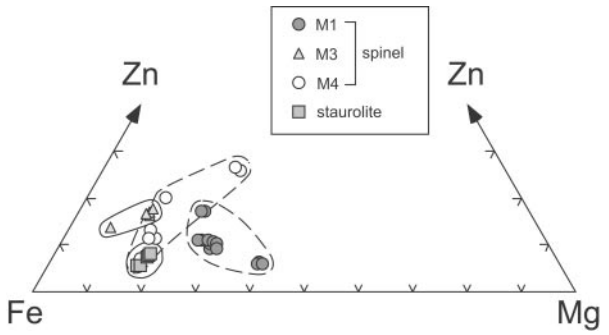

Fig. 8. Fe–Mg–Zn ternary plot of spinel and staurolite compositions in pelitic granulites.

that they preserve peak metamorphic compositions. Temperatures estimated from two-pyroxene geothermometry (Anderson & Lindsley, 1988), using the integrated compositions of pyroxenes, vary from 791 to 799°C at an assumed pressure of 7 kbar (Table 9; Fig. 9a). For garnet–orthopyroxene–plagioclase–quartz assemblages, P–T conditions were estimated using both conventional (Harley & Green, 1982; Moecher *et al.*, 1988) and multi-equilibrium (TWQ; Berman, 1991) geothermobarometers. The former, using the calibrations of Harley & Green (1982) and Moecher *et al.* (1988), yielded the P–T condition of 6·4–8·8 kbar and 711–842°C (Table 9; Fig. 9a). To minimize the effect of post-metamorphic compositional adjustment between garnet and orthopyroxene (Fitzsimons & Harley, 1994), the calibration of Harley & Green (1982), based on the solubility of alumina in orthopyroxene coexisting with garnet, was adopted. The P–T conditions estimated from the TWQ software (Berman, 1991) with the internally consistent thermodynamic set updated by Aranovich & Berman (1997) are in the range of 5·5–7·6 kbar and 684–884°C for the garnet–orthopyroxene–plagioclase–quartz assemblage (Table 9; Fig. 9a). Low temperatures estimated for some samples (e.g. HC87 and HC87′) may reflect the effect of retrograde Fe–Mg exchange. By excluding these samples, the P–T estimates are 7·8 ± 0·7 kbar and 827 ± 29°C, and 6·9 ± 0·9 kbar and 814 ± 61°C, respectively, for both calibrations. These results corroborate those of the two-pyroxene geothermometer.

The M_2 assemblage of pelitic granulites is represented by garnet + sillimanite ± biotite + K-feldspar + plagioclase + quartz, and their pressure conditions were estimated from the assemblage garnet–sillimanite–plagioclase–quartz, following the calibration of Koziol (1989). When the core compositions of primary garnet and plagioclase are used at an assumed temperature of 800°C, the calibration of Koziol (1989) yields pressure estimates varying from 7·1 to 9·1 kbar in leucocratic gneisses and from 8·4 to 10·7 kbar in kyanite–garnet and aluminous gneisses (Table 9; Fig. 9a). Thus, average pressures are 7·6 ± 1·0 kbar for the leucocratic gneisses and 9·5 ± 1·0 kbar for the kyanite–garnet and aluminous gneisses. When the occurrence of kyanite inclusions in kyanite–garnet and aluminous gneisses is taken into account, the higher pressure of the latter is consistent with the field occurrence and mineralogical evidence. In addition, the pressures estimated from the leucocratic gneiss are consistent with those from the mafic granulite.

Pressures and temperatures attending peak granulite-facies metamorphism coincide with the experimentally determined conditions for fluid-absent melting of pelitic rocks (e.g. LeBreton & Thompson, 1988; Vielzeuf & Holloway, 1988; Stevens *et al.*, 1997), and are corroborated by the abundance of garnetiferous leucogranites in the HGC. Garnet grains enclosing biotite, sillimanite, rare kyanite, plagioclase and quartz in migmatitic leucosomes and leucogranites indicate that these granitic bodies are the product of dehydration-melting reactions consuming biotite. Thus, the following reactions may account for the occurrence of garnet-bearing anatectic melts in pelitic granulites:

$$\text{biotite} + \text{sillimanite (or kyanite)} + \text{plagioclase} + \text{quartz} = \text{garnet} + \text{K-feldspar} + \text{melt} \quad (1)$$

in Al-silicate-bearing rocks, and

$$\text{biotite} + \text{plagioclase} + \text{quartz} = \text{garnet} + \text{K-feldspar} + \text{melt} \quad (2)$$

in Al-silicate-free rocks, respectively. Except for kyanite–garnet and aluminous gneisses, the reactions (1) and (2) have occurred mainly within the stability field of sillimanite. Equilibrium relationships among biotite, sillimanite, quartz, garnet and K-feldspar were used to calculate the activity of H_2O (a_{H_2O}) in pelitic granulites relative to the standard state defined as pure H_2O at P and T using the method of Phillips (1980). Calculated activities range from 0·09 to 0·32 (Table 10), suggesting that widespread anatexis occurred under low a_{H_2O} conditions. These low a_{H_2O} values are consistent with those reported from granulite terranes that have experienced fluid-absent melting (e.g. Young *et al.*, 1989; Braun *et al.*, 1996). In addition to melting reactions (1) and (2), rare garnet coexisting with corundum aggregates encloses hercynite and sillimanite, suggesting the following silica-deficient reaction:

$$\text{hercynite} + \text{sillimanite} = \text{garnet} + \text{corundum}. \quad (3)$$

Because this reaction has a gently positive slope in P–T space (Bohlen *et al.*, 1986), the growth of some M_2 garnets was extended to the waning (or incipient cooling) stage

Table 9: Summary of P–T *estimates for* M_2

Sample no.	Opx				Cpx			Grt				P_1	T_1	$T_2(P_1)$	$T_3(P_2)$	P_3
	X_{En}	X_{Wo}	X_{Fs}	X_{Ok}	X_{En}	X_{Wo}	X_{Fs}	X_{Alm}	X_{Prp}	X_{Sps}	X_{Grs}	X_{An}				
TPX													*at 7 kbar*			
HC84B	0·472	0·020	0·508			0·352	0·426	0·221					797			
HC85G	0·333	0·028	0·639			0·262	0·432	0·306					791			
GOPQ																
HC85A	0·485		0·466	0·035				0·679	0·246	0·014	0·061	0·499		842 (7·2)	740 (5·5)	
HC85E	0·421		0·527	0·024				0·694	0·189	0·016	0·101	0·469		784 (7·5)	796 (7·0)	
HC85E′	0·477		0·466	0·030				0·682	0·210	0·012	0·096	0·458		840 (8·8)	708 (6·6)	
HC87	0·379		0·598	0·013				0·648	0·115	0·010	0·227	0·862		711 (6·6)	834 (7·3)	
HC87′	0·435		0·518	0·020				0·704	0·159	0·018	0·119	0·726		724 (6·4)	684 (5·6)	
YK5D2	0·469		0·489	0·032				0·637	0·252	0·026	0·085	0·501		842 (7·8)	884 (7·6)	
GASP																*at 800°C*
HC19-1B								0·587	0·368	0·007	0·038	0·298				9·2
HC22-1								0·597	0·354	0·012	0·037	0·311				8·9
HC78								0·672	0·287	0·013	0·027	0·278				8·0
HC79-6								0·630	0·317	0·013	0·040	0·339				8·7
HC83B								0·708	0·250	0·015	0·027	0·267				8·0
HC85B								0·673	0·277	0·015	0·035	0·220				10·5
HC85D								0·668	0·302	0·007	0·024	0·286				7·3
HC130C								0·630	0·320	0·013	0·037	0·325				8·9
HY21								0·717	0·234	0·017	0·031	0·351				7·1
YK19								0·633	0·315	0·013	0·040	0·311				9·1
YK23								0·612	0·348	0·012	0·029	0·181				11·0
YK51B								0·625	0·309	0·009	0·056	0·312				10·7
YK51C2								0·637	0·316	0·011	0·035	0·327				8·4

TPX, two-pyroxene; GOPQ, garnet–orthopyroxene–plagioclase–quartz; GASP: garnet–Al-silicate–plagioclase–quartz. T_1, Anderson & Lindsley (1988); T_2, Harley & Green (1982); T_3, TWQ (Berman, 1991); P_1, Moecher *et al.* (1988); P_2, TWQ; P_3, Koziol (1989).

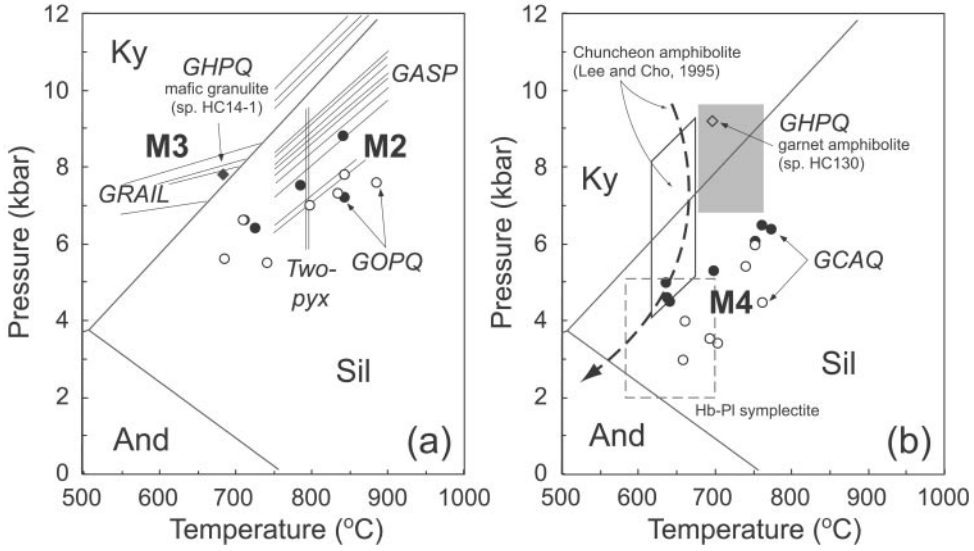

Fig. 9. *P–T* conditions estimated for metamorphic stages M_2 and M_3 (a), and M_4 (b). Abbreviations: Two-pyx, two-pyroxene geothermometer (Anderson & Lindsley, 1988); GOPQ, garnet–orthopyroxene–plagioclase–quartz. In (a): ●, *P–T* estimates from the combination of the Harley & Green (1982) geothermometer, based on the solubility of alumina in orthopyroxene coexisting with garnet, and the GOPQ geobarometer of Moecher *et al.* (1988). ○, *P–T* estimates from the multi-equilibrium geothermobarometry (Berman, 1991); GASP, garnet–sillimanite–plagioclase–quartz geobarometer (Koziol, 1989); GCAQ, garnet–cordierite–sillimanite–quartz. In (b): ●, *P–T* estimates from the combination of garnet–cordierite geothermometer (Perchuk & Lavren'teva, 1983) and GCAQ geobarometer (Aranovich & Podlesskii, 1983). ○, *P–T* estimates from multi-equilibrium geothermobarometer (Berman, 1991); GRAIL, garnet–rutile–kyanite–ilmenite–quartz geobarometer (Bohlen *et al.*, 1983); GHPQ, garnet–hornblende–plagioclase–quartz geobarometer (Kohn & Spear, 1990), together with temperatures estimated from the garnet–hornblende geothermometer (Graham & Powell, 1984). ◆, mafic granulite (HC14-1); ◇, garnet amphibolite (HC130). Grey and dashed boxes represent the *P–T* conditions for garnet amphibolites and hornblende–plagioclase symplectites, respectively, reported in the HGC by Yi (1998). Open box and dashed curve denote the *P–T* conditions and *P–T* path of the Chuncheon amphibolites, MZGC (Lee & Cho, 1995). Reaction curves between kyanite (Ky), sillimanite (Sil) and andalusite (And) are from Holdaway (1971).

of M_2 metamorphism, especially in silica-deficient regions induced by partial melting.

M_3 metamorphism

The occurrence of M_3 kyanite is characteristic for the retrogression of pelitic granulites. Kyanite commonly occurs in kyanite–garnet and aluminous gneisses, and rarely in leucocratic gneisses. Kyanite primarily occurs in the matrix as corroded grains, together with rare rutile and staurolite, replacing M_2 garnet porphyroblasts. However, a few grains of M_3 kyanite also occur along fractures in M_2 garnet porphyroblasts and commonly replace acicular sillimanite. These textural features suggest that the following reactions were operative:

$$\text{garnet} + \text{K-feldspar} + H_2O = \text{biotite} + \text{sillimanite (or kyanite)} + \text{plagioclase} + \text{quartz} \quad (4)$$

and

$$\text{sillimanite} = \text{kyanite}. \quad (5)$$

In addition, the formation of M_3 staurolite in the kyanite–garnet gneiss may be attributed to the following hydration reaction:

$$\text{garnet} + \text{sillimanite (or kyanite)} + H_2O = \text{staurolite} + \text{quartz}. \quad (6)$$

In conjunction with reaction (3), the formation of kyanite and staurolite can be inferred to result from a fall in temperature along a quasi-isobaric cooling path.

The quasi-isobaric cooling path inferred from the pelitic granulites is compatible with the formation of garnet coronas in mafic granulites. The garnet coronas occur as thin, continuous bands between plagioclase and ortho- or clinopyroxene, and are commonly interspaced with cummingtonite–hornblende–quartz symplectites around pyroxenes. The formation of garnet coronas at the expense of pyroxene is attributed to the following reactions:

$$\text{orthopyroxene} + \text{plagioclase} = \text{garnet} + \text{quartz} \quad (7)$$

and

$$\text{clinopyroxene} + \text{plagioclase} = \text{garnet} + \text{quartz}. \quad (8)$$

In addition to these pressure-sensitive reactions, interstitial growth of amphibole around pyroxenes indicates that partial hydration reactions have occurred in the presence of limited fluid. The formation of garnet coronas and partial hydration of pyroxene are the reaction textures characteristic for many isobarically cooled granulite

Table 10: H_2O activities calculated using the method of Phillips (1980)

Sample no.	Biotite				Garnet		K-feldspar	a_{H_2O}*
	X_{Fe}	X_K	X_{OH}	a_{Ann}	X_{Fe}	a_{Alm}	a_{Ksp}	
HC19-1B	0·245	0·983	0·976	0·014	0·605	0·221	0·870	0·32
HC22-1	0·197	0·967	0·995	0·007	0·627	0·246	0·843	0·16
HC78	0·184	0·975	0·997	0·006	0·636	0·257	0·849	0·12
HC79-3	0·225	0·974	<1	<0·011	0·649	0·273	0·700	<0·26
HC79-6	0·180	0·972	<1	<0·006	0·653	0·278	0·756	<0·12
HC83Bb	0·187	0·979	0·989	0·006	0·739	0·404	0·778	0·09
HC85D	0·214	0·977	0·996	0·009	0·689	0·327	0·767	0·17
HY7	0·264	0·982	0·876	0·014	0·666	0·295	0·914	0·23
YK42-3	0·227	0·963	<1	<0·011	0·702	0·346	0·852	<0·17

*H_2O activities estimated from the reaction annite + sillimanite + 2quartz = almandine + K-feldspar + H_2O.

terranes (e.g. Harley, 1989; Zhao *et al.*, 2001). This isobaric cooling path is compatible with that inferred from pelitic granulites.

P–T conditions of the M_3 stage were estimated from the garnet–hornblende–plagioclase–quartz assemblage of mafic granulite, and from the garnet–rutile–kyanite–ilmenite–quartz assemblage of the pelitic granulites. For the latter, rim compositions of fragmentary M_2 garnet were used. The *P–T* conditions from coronitic garnet and hornblende in retrogressive mafic granulite (sample HC14-1) were estimated to be 7·8 kbar and 689°C, using the garnet–hornblende geothermometer (Graham & Powell, 1984) and garnet–hornblende–plagioclase–quartz geobarometer (Kohn & Spear, 1990) (Table 11; Fig. 9b). Pressures estimated from the garnet–rutile–kyanite–ilmenite–quartz geobarometer (Bohlen *et al.*, 1983) are in the range of 7·2–8·4 kbar at 700°C (Table 11). The *P–T* conditions estimated for M_3 lie in the kyanite stability field, corroborating the occurrence of M_3 kyanite in the pelitic granulites.

M_4 metamorphism

The M_4 stage is characterized by the growth of cordierite that replaces the M_2 and M_3 assemblages in the pelitic granulites. Cordierite enclosing M_2 garnet and sillimanite/kyanite is produced by the following reaction:

$$\text{garnet} + \text{kyanite/sillimanite} + \text{quartz} \; (+ \text{fluid}) = \text{cordierite}. \quad (9)$$

The occurrence of ilmenite enclosing rutile is attributed to the following reaction:

$$\text{garnet} + \text{rutile} = \text{kyanite} + \text{ilmenite} + \text{quartz}. \quad (10)$$

Because both reactions (9) and (10) are sensitive to pressure changes (Holdaway & Lee, 1977; Bohlen *et al.*, 1983; Mukhopadhyay & Holdaway, 1993), the M_4 stage is the product of apparent decompression. However, the occurrence of cordierite occurring as isolated patches replacing residual biotite, and locally coexisting with M_4 garnet, suggests that the following dehydration reactions are also operative during decompression:

$$\text{biotite} + \text{sillimanite} + \text{plagioclase} + \text{quartz} \; (+ \text{fluid}) = \text{cordierite} + \text{K-feldspar} + H_2O \quad (11)$$

and

$$\text{biotite} + \text{sillimanite} + \text{plagioclase} + \text{quartz} \; (+ \text{fluid}) = \text{garnet} + \text{cordierite} + \text{K-feldspar} + H_2O. \quad (12)$$

The *P–T* conditions of M_4 were estimated using the assemblage garnet–sillimanite–cordierite–quartz in pelitic granulites. Because of the large uncertainty in the pressure estimation using cordierite with an unknown fluid content, we adopted an average value of estimations for both 'wet' and 'dry' conditions of cordierite. The resulting *P–T* estimates are in the range of 3·0–6·0 kbar and 657–760°C, using the calibrations of Perchuk & Lavren'teva (1983) and Aranovich & Podlesskii (1983) (Table 11; Fig. 9b). On the other hand, multi-equilibrium geothermobarometry (Berman, 1991) yields *P–T* conditions of 4·5–6·5 kbar and 638–775°C, respectively, assuming 'wet' conditions in cordierite (Table 11; Fig. 9b). The significant variations in *P–T* estimates can be attributed to the large extrapolation required for using garnet–cordierite thermobarometry, the unknown fluid content of cordierite, and variable retrograde Fe–Mg exchange. In particular, the effect of retrograde exchange reaction between garnet and cordierite is prominent in kyanite–garnet gneiss.

Table 11: Summary of P–T *estimates for* M_3 *and* M_4

Sample no.	Grt				Pl	Crd	Hb			Ilm	T_4 (P_4)	T_5 (P_5)	T_6 (P_6)	P_7
	X_{Alm}	X_{Prp}	X_{Sps}	X_{Grs}	X_{An}	X_{Fe}	X_{T1Si}	X_{T1Al}	X_{Fe}	X_{Fe}				
M_3 metamorphism														
GHPQ														
HC14-1	0·595	0·177	0·014	0·213	0·362		0·648	0·352	0·461				689 (7·8)	
GRAIL														*at 700°C*
HC19-1B	0·707	0·249	0·014	0·030						0·970				7·2
HC130C	0·792	0·131	0·044	0·033						0·982				8·1
YK51B	0·799	0·138	0·026	0·036						0·978				8·4
YK51C2	0·775	0·175	0·017	0·034						0·985				8·0
YK101	0·771	0·189	0·013	0·028						0·994				7·9
M_4 metamorphism														
GHPQ														
HC130	0·571	0·103	0·030	0·295	0·408		0·583	0·417	0·543				697 (9·2)	
GCSQ														
HC83B	0·738	0·215	0·014	0·033		0·343					740 (6·1)	755 (6·1)		
HC85B	0·695	0·250	0·014	0·041		0·304					755 (6·4)	764 (6·5)		
HC85D	0·770	0·165	0·009	0·057		0·340					760 (6·2)	775 (6·4)		
YK19	0·742	0·158	0·016	0·084		0·292					690 (5·3)	636 (5·0)		
HC130C	0·792	0·131	0·044	0·033		0·375					657 (4·7)	638 (4·6)		
YK51B	0·799	0·138	0·026	0·036		0·359					703 (5·2)	699 (5·3)		
YK51C2	0·775	0·175	0·017	0·034		0·361					662 (4·6)	641 (4·5)		

GHPQ, garnet–hornblende–plagioclase–quartz; GRAIL, garnet–rutile–Al-silicate–ilmenite–quartz; GCSQ, garnet–cordierite–sillimanite–quartz. T_4, Perchuk & Lavren'teva (1983); T_5 and P_5, TWQ (Berman, 1991); T_6, Graham & Powell (1984); P_4, Aranovich & Podlesskii (1983); P_6, Kohn & Spear (1990); P_7, Bohlen *et al.* (1983).

The P–T conditions for the onset of M_4 are difficult to estimate in the absence of geochronologic information for discerning M_3 and M_4 assemblages. However, M_4 is interpreted to be responsible for the development of garnet-bearing assemblages in the type 2 amphibolites (sample HC130) that were emplaced subsequent to M_2 and M_3. The P–T conditions of such a garnet amphibolite were estimated to be ~9·2 kbar and 700°C, using the garnet–hornblende geothermometer (Graham & Powell, 1984) and garnet–hornblende–plagioclase–quartz geobarometer (Kohn & Spear, 1990) (Table 11; Fig. 9b). Overall, the M_4 event is characterized by the formation of symplectites consisting of hornblende and plagioclase at garnet margins. This texture, together with the presence of quartz near the symplectite, suggests the growth of hornblende at the expense of garnet and quartz by the following continuous reaction:

garnet + hornblende + quartz = less aluminous hornblende + plagioclase. (13)

The gentle positive dP/dT slope of reaction (13) (e.g. Kohn & Spear, 1990) suggests that the hornblende–plagioclase symplectite in the garnet amphibolites has formed by recrystallization during decompression. P–T conditions for the symplectite formation were estimated from three garnet amphibolite samples by Yi (1998) to be in the range of ~2–5 kbar and 580–700°C. This result is consistent with that calculated from cordierite-bearing pelitic granulites, suggesting a decompression of ~4–7 kbar during the M_4 metamorphism.

M_5 metamorphism

After the M_4 stage, further thermal disturbance is apparent because of the local growth of andalusite in some pelitic granulites. Andalusite mantles secondary garnet in the banded biotite gneiss of the MZGC adjacent to a Jurassic granitoid batholith. Thus, rare andalusite in the HGC is interpreted to result from the thermal effects of intrusion of this granitoid.

DISCUSSION

Pressure–temperature–time evolution

A composite P–T path for the metamorphic evolution of HGC was deduced on the basis of mineral inclusion relationships, reaction textures and geothermobarometry. Two clockwise P–T trajectories apparently occur at relatively high and low temperatures, respectively (Fig. 10). Moreover, available geochronologic data suggest that these P–T trajectories cannot be accounted for by a single tectonothermal event, but by multiple events unrelated to each other (Ellis, 1987; Harley, 1989, 1992; Bohlen, 1991).

The first trajectory (M_1–M_3), responsible for the formation of granulites, has been dated at 1872 ± 7 Ma by ion microprobe U–Pb analyses of zircon in a migmatitic leucocratic gneiss (Lee *et al.*, 2000). In addition, U–Pb zircon ages are identical for leucosome and melanosome, suggesting that the granulite-facies metamorphism and partial melting are synchronous.

The second trajectory (M_4) has not been precisely dated yet, but appears to be related to Permo-Triassic orogenesis because the CHIME (chemical U–Th–total Pb isochron method) monazite ages of ~255–240 Ma are prevalent in a wide area covering both the HGC and the MZGC (Cho *et al.*, 1996; Suzuki & Adachi, 1999). These ages were obtained largely from the overgrowth domains mantling Palaeoproterozoic monazite cores, suggesting that monazite has recrystallized at the upper amphibolite-facies condition during M_4. On the other hand, a preliminary CHIME monazite age of ~220 Ma, reported from a mylonitic granulite near the HGC–MZGC boundary (Yi *et al.*, 2001), indicates that extensional shearing movement occurred during Triassic time. These Permo-Triassic growths of monazite are compatible with $^{40}Ar/^{39}Ar$ ages of hornblende in garnet amphibolite (226 ± 8 Ma), and muscovite in a deformed pegmatite (202 ± 4 Ma; Cho *et al.*, 1999). Taken together, these geochronologic data attest to the superimposition of upper amphibolite-facies Permo-Triassic metamorphism on Palaeoproterozoic granulite-facies metamorphism in the HGC.

Following the M_4 regional metamorphism and subsequent cooling, local thermal perturbation (M_5) has occurred in association with the Jurassic granitoids. Porphyritic granite and hornblende gabbro in the MZGC yield U–Pb zircon ages of 164·7 ± 2·4 Ma and 166·2 ± 1·2 Ma, respectively (Kim *et al.*, 1999). Thus, M_5 thermal metamorphism is attributed to the Jurassic thermal event unrelated to M_4.

Palaeoproterozoic evolution of the HGC

The Palaeoproterozoic metamorphic episode defines a clockwise P–T path, consisting of prograde heating, thermal peak, and subsequent quasi-isobaric cooling (Fig. 10). The rare occurrence of kyanite inclusions in M_2 garnet from pelitic granulites shows that the onset of prograde (M_1) metamorphism occurred within the kyanite stability field, and suggests crustal thickening before the granulite-facies metamorphism. However, the predominance of sillimanite in pelitic granulites indicates that sillimanite was the stable Al-silicate at the thermal peak (M_2). Moreover, the general absence of garnet–clinopyroxene assemblages in the mafic granulites indicates that the peak temperatures were reached at

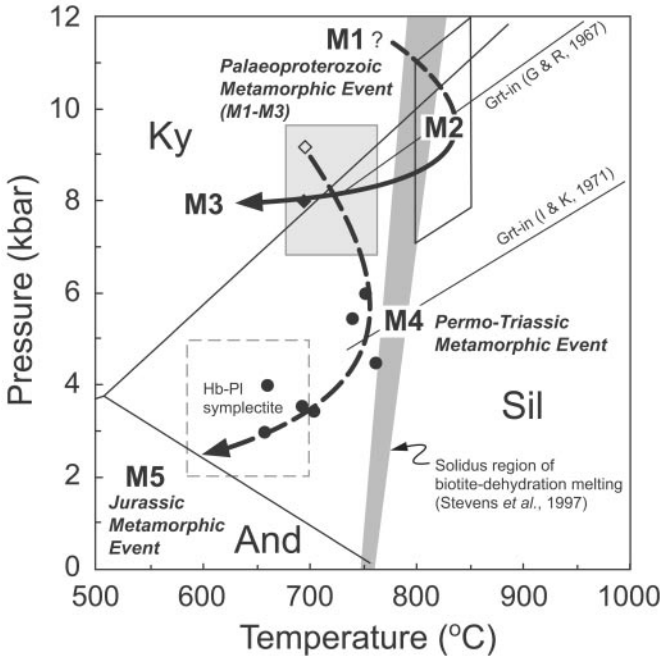

Fig. 10. *P–T* diagram showing two clockwise trajectories resulting from Palaeoproterozoic (M_1 to M_3) and Permo-Triassic (M_4) tectonometamorphic events, respectively. Grey and dashed boxes represent the *P–T* conditions estimated from the GHPQ assemblages and hornblende–plagioclase symplectites in garnet amphibolites, respectively (Yi, 1998). Solidus region of biotite-dehydration melting in pelitic rocks is adopted from Stevens *et al.* (1997). The peak metamorphic conditions, exceeding the solidus region of dehydration melting in pelitic rocks, are consistent with the widespread occurrence of migmatitic gneisses and garnet-bearing leucogranites. Garnet-in reactions for quartz tholeiite and olivine basalt are adopted from Green & Ringwood (1967) and Ito & Kennedy (1971), respectively. Reaction curves among kyanite (Ky), sillimanite (Sil) and andalusite (And) are from Holdaway (1971).

medium-pressure conditions (Green & Ringwood, 1967). These observations suggest that the thermal peak postdates the major compressional thickening and has occurred during denudation of the thickened crust.

Peak (M_2) metamorphism exceeded the conditions necessary for dehydration-melting of pelitic rocks, and granulite-facies metamorphism was accompanied by widespread partial melting that produced locally abundant leucogranite (Fig. 10; Stevens *et al.*, 1997). Despite the voluminous production of granitic melts, significant intracrustal differentiation is lacking in the HGC, probably because the extraction and ascent of granitic magmas were hampered by the concomitant ascent of residual host gneisses (Sawyer, 1994). This ascending process resulted in a migmatitic complex comprising both metatexite and diatexite, but was terminated at mid-crustal depths (~25–30 km).

The retrograde *P–T* path of the granulite-facies metamorphism is recorded by the development of M_3 assemblages (e.g. secondary kyanite and garnet corona in pelitic and mafic granulites, respectively). Although no direct constraints on the timing of the M_3 metamorphism are yet available, the lack of deformation-related growth of M_3 minerals suggests that this metamorphic stage represents the final stage of the Palaeoproterozoic metamorphic event associated with adjustment to a steady-state geotherm during thermal relaxation and cooling. The M_3 minerals occur only locally because of the sluggish kinetics of retrograde reaction in the absence of a fluid phase and/or deformation (Harley, 1989; Ellis & Maboko, 1992; Hensen *et al.*, 1995). It is rather common to find granulites that have cooled isobarically into the kyanite stability field before final exhumation (Bohlen, 1987; Harley, 1989; Ellis & Maboko, 1992).

Heat source for the granulite formation

The HGC experienced a typical clockwise *P–T* path, which involves deep burial of supracrustal rocks and subsequent thermal relaxation, followed by quasi-isobaric cooling. Such a path is commonly assumed to be typical of the lower continental mass in a crustal section doubled in thickness by collision (England & Thompson, 1984; Ellis, 1987; Chapman & Furlong, 1992). Collisional thickening may therefore account for the formation of the HGC. However, thermal models using reasonable values for thermal conductivity, crustal heat production and basal heat flux predict that such *P–T* paths should lie

within the kyanite stability field (England & Thompson, 1984; Thompson, 1990; De Yoreo *et al.*, 1991; Chapman & Furlong, 1992). As a consequence, the attainment of the granulite-facies condition within the sillimanite stability field requires an additional heat source.

Advective heat transport from the mantle by underplating of mafic magmas has been commonly proposed as the mechanism to allow attainment of granulite-facies conditions within the sillimanite stability field in regions of thickened crust (Bohlen, 1987; Harley, 1989; De Yoreo *et al.*, 1991; Thompson & Connolly, 1995). In addition, anomalously high basal heat flow may result from lithospheric extension before thickening, or large-scale infiltration of hot fluids (Chamberlain & Rumble, 1988). Pre-thickening input of heat is unlikely for the HGC, because kyanite and staurolite occur as relict minerals. On the other hand, large-scale fluid infiltration is not consistent with the widespread anatexis by fluid-absent dehydration melting observed in pelitic granulites.

Advective heating could be a consequence of either lithospheric delamination (Bird, 1979; Houseman *et al.*, 1981) or convective thinning of thickened lithosphere (Loosveld & Etheridge, 1990; Sandiford & Powell, 1990, 1991). These processes may cause an increase in magmatism, variation in magma composition, rapid uplift, and a change in stress regime from compression to extension (Kay & Kay, 1993; Rudnick, 1995). In addition, large-scale granulite-facies metamorphism occurs only if the volume of accreted magma is similar to or greater than the volume of the pre-existing crust, and requires a major period of crustal growth (Wells, 1980; Bohlen, 1987; Huppert & Sparks, 1988; Bergantz, 1989; Oxburgh, 1990). In the northeastern Gyeonggi massif, however, no evidence for voluminous magmatism is apparent at $\sim$1·87 Ga. Furthermore, Nd-depleted mantle model (T_{DM}) ages of pelitic granulites suggest a major accretion of juvenile materials at 2·8–2·6 Ga (Lee *et al.*, 2000). Thus, in lieu of advective heating through mantle magmatism, widespread anatexis could be merely a reflection of the heating that caused the granulite-facies metamorphism (Wickham, 1987; Thompson, 1989).

Alternatively, the granulite-facies conditions may be attained by the burial of layers containing high concentrations of heat-producing elements (K, U and Th) during crustal thickening (De Yoreo *et al.*, 1989; Chamberlain & Sonder, 1990; Patiño Douce *et al.*, 1990; Buick *et al.*, 1998; Gerdes *et al.*, 2000). Chamberlain & Sonder (1990) showed that, in the absence of abnormal mantle heat flow or heat advection by magma emplacement, burial of high heat-producing layers could result in the attainment of upper amphibolite- to lower granulite-facies conditions by thermal relaxation during compressional orogenesis. The present-day concentrations of heat-producing elements in pelitic granulites of the HGC were estimated by Yi (1998) as 1·70 $\pm$ 0·92 ppm U, 31·0 $\pm$ 13·6 ppm Th and 2·63 $\pm$ 0·33 wt % K. Thus, the average radiogenic heat production is 3·0 $\pm$ 1·2 mW/m^3. This value is higher than the radiogenic heat production of average upper continental crust [$\sim$1·8 mW/m^3; calculated from Taylor & McLennan (1985)]. On the other hand, it is comparable with $\sim$2–3 mW/m^3 estimated from the metasedimentary protoliths of post-orogenic granites in the Variscan collision zone, characterized by high-temperature metamorphism associated with crustal magmatism (Gerdes *et al.*, 2000). Therefore, although the variation of heat production with depth in sedimentary protoliths of granulites is poorly constrained, we tentatively propose that abnormally high internal heat production made an important thermal contribution to the granulite-facies metamorphism in the HGC.

Permo-Triassic exhumation of the HGC

Subsequent to M_3, the HGC resided at mid- to upper-crustal depths for a prolonged time before the Permo-Triassic crustal-thickening event (M_4). This reactivation of the HGC is characterized by a quasi-isothermal decompression (ITD) path, accounting for the growth of cordierite in pelitic granulites and hornblende–plagioclase symplectites in garnet amphibolites. Moreover, high-pressure conditions of type 2 amphibolites suggest that the decompression was initiated from the kyanite stability field. This inference is also supported by near-isothermal decompression along a clockwise *P–T* path reported from garnet amphibolites of the Chuncheon area, southern MZGC (Lee & Cho, 1995) (Fig. 9b). Although most rock types show little evidence for significant overprinting of M_4, cordierite-bearing gneisses and garnet amphibolites suggest the wholesale denudation of the HGC at $\sim$700°C. This decompressional process is probably triggered by upward movement along ductile thrusts and shear zones that separate the HGC from the MZGC (Lee *et al.*, 2000) (Fig. 2). The majority of compressional shear zones are severely overprinted by later extensional, ductile deformation, suggesting gravitational collapse of the thickened crust (Lee *et al.*, 2000). Thus, these shear zones preserve structural and metamorphic records of exhumation from depths of $\sim$30 km to 10–15 km. Such decompressional paths caused by compressional exhumation along major thrusts or ductile shear zones have been also proposed for some reworked granulite terranes within collisional orogens (e.g. Schenk, 1984; Sandiford, 1985; Currie & Gittins, 1988; Percival *et al.*, 1992).

Tectonic implications for crustal evolution of East Asia

The discovery of a coherent volume of granulite-facies rocks, characterized by a collision-related orogenic event

of Palaeoproterozoic age, provides an important constraint on the tectonic evolution of the Gyeonggi massif. The basement rocks of the Gyeonggi massif are traditionally considered as the product of Archaean to Palaeoproterozoic low-P/high-T thermal regimes (Lee, 1987). However, relict grains of kyanite observed throughout the Gyeonggi massif (Lee & Cho, 1992; Cho & Kim, 1993; Cho *et al.*, 1995; Ahn *et al.*, 1998) suggest that high- to medium-pressure conditions were attained before the widespread low-P/high-T metamorphism. In light of our results, the occurrence of relict kyanite suggests that the collisional orogeny has affected not only supracrustal rocks but also basement rocks of the Gyeonggi massif.

Temporal and tectonic relationships for the exhumation of Palaeoproterozoic granulites indicate that thick-skinned crustal reworking has occurred in the Gyeonggi massif, possibly during the Permo-Triassic. The northern margin of the Gyeonggi massif is bounded by the east-trending Imjingang belt, which has also experienced the Permo-Triassic thermotectonic event (Cho *et al.*, 1995; Ree *et al.*, 1996). The Imjingang belt has been interpreted as an eastward extension to the Korean Peninsula of the ultrahigh-pressure continental collision belt between the Yangtze and Sino-Korean cratons (Yin & Nie, 1993; Li, 1994; Cho *et al.*, 1995; Ree *et al.*, 1996). Our results further suggest that the northern margin of the Gyeonggi massif has experienced compressional tectonic processes during the Permo-Triassic, coeval with the timing of continental collision in east–central China (Ames *et al.*, 1993, 1996; Li *et al.*, 1993; Eide *et al.*, 1994). Therefore, it is likely that the northern Gyeonggi massif as well as the Imjingang belt have participated in the Permo-Triassic tectonic process correlative to the continental collision between the Yangtze and Sino-Korean cratons.

CONCLUSIONS

The granulite complex in the Hwacheon area, northeastern Gyeonggi massif, consists of migmatitic granulites enclosing minor mafic granulite and garnet amphibolites. The mineral parageneses and reaction textures indicate that the granulite complex has experienced two metamorphic events, in association with collisional crustal thickening, in Palaeoproterozoic ($\sim$1·87 Ga) and Permo-Triassic ($\sim$255–240 Ma) times, respectively. The peak metamorphic conditions during the earlier collisional event were estimated to be in the range of $\sim$7·0–9·5 kbar and 790–830°C, whereas the second metamorphic event reached P–T conditions of $\sim$3–6 kbar and 660–750°C.

The burial of sedimentary protoliths enriched in heat-producing elements may have resulted in granulite-facies metamorphism and widespread partial melting during the Palaeoproterozoic crustal-thickening orogeny. The occurrence of M_3 kyanite and garnet coronas in pelitic and mafic granulites, respectively, indicate that the HGC cooled near-isobarically following granulite-facies metamorphism and resided at mid-crustal depths before final exhumation. The second tectonometamorphism defined by the ITD path is attributed to reactivational exhumation during the Permo-Triassic compressional orogeny which is prevalent in Far-East Asia.

ACKNOWLEDGEMENTS

This paper represents a part of a Ph.D. thesis of the senior author at Seoul National University, and the field assistance of our colleagues, in particular Keewook Yi, is greatly appreciated. We thank Ian Fitzsimons and Simon Johnson for critically reviewing an early version of the manuscript. We also thank the journal reviewers Ian Buick, Chris Carson, Simon Harley and Michael Raith for their helpful and constructive comments that greatly improved the clarity of this paper. This study was supported by Korea Research Foundation Grant (KRF-2001-041-D00255) to M.C.

REFERENCES

Ahn, K. S., Park, Y. S., Kim, J. B. & Chen, J. (1998). Metamorphism of gneiss complex in the Paju-Gimpo area, northwestern Gyeonggi massif, Korea. *Journal of Petrological Society of Korea* **7**, 177–189.

Ames, L., Tilton, G. R. & Zhou, G. (1993). Timing of collision of the Sino-Korean and Yangtze cratons: U–Pb zircon dating of coesite-bearing eclogites. *Geology* **21**, 339–342.

Ames, L., Zhou, G. Z. & Xiong, B. C. (1996). Geochronology and isotopic character of ultrahigh-pressure metamorphism with implications for collision of the Sino-Korean and Yangtze cratons, central China. *Tectonics* **15**, 472–489.

Anderson, D. J. & Lindsley, D. L. (1988). Internally consistent solution models for Fe–Mg–Mn–Ti oxides: Fe–Ti oxides. *American Mineralogist* **73**, 714–726.

Aranovich, L. & Podlesskii, K. K. (1983). The cordierite–garnet–sillimanite–quartz equilibrium: experiments and applications. In: Saxena, S. K. (ed.) *Advances in Physical Geochemistry, Kinetics and Equilibrium in Mineral Reactions, 3*. New York: Springer, pp. 172–198.

Aranovich, L. Y. & Berman, R. G. (1997). Optimized standard state and solution properties of minerals. II. Comparisons, predictions, and applications. *Contributions to Mineralogy and Petrology* **126**, 25–37.

Bergantz, G. W. (1989). Underplating and partial melting: implications for melt generation and extraction. *Science* **245**, 1093–1094.

Berman, R. G. (1991). Thermobarometry using multi-equilibrium calculations: a new technique, with petrological applications. *Canadian Mineralogist* **29**, 833–855.

Bird, P. (1979). Continental delamination and the Colorado Plateau. *Journal of Geophysical Research* **84**, 7561–7571.

Bohlen, S. R. (1987). Pressure–temperature–time paths and a tectonic model for the evolution of granulites. *Journal of Geology* **95**, 617–632.

Bohlen, S. R. (1991). On the formation of granulites. *Journal of Metamorphic Geology* **9**, 223–229.

Bohlen, S. R., Wall, V. J. & Boettcher, A. L. (1983). Experimental investigations and geological applications of equilibria in the system FeO–TiO_2–Al_2O_3–SiO_2–H_2O. *American Mineralogist* **68**, 1049–1058.

Bohlen, S. R., Dollase, W. A. & Wall, V. J. (1986). Calibration and application of spinel equilibria in the system FeO–Al_2O_3–SiO_2. *Journal of Petrology* **27**, 1143–1156.

Braun, I., Raith, M. & Kumar, R. R. (1996). Dehydration-melting phenomena in leptynitic gneisses and the generation of leucogranites: a case study from the Kerala Khondalite Belt, southern India. *Journal of Petrology* **37**, 1285–1305.

Brown, M. (1973). The definition of metatexis, diatexis and migmatite. *Proceedings of the Geologists' Association* **84**, 371–382.

Brown, M. (1993). *P–T–t* evolution of orogenic belts and the causes of regional metamorphism. *Journal of the Geological Society, London* **150**, 227–241.

Buick, I. S., Cartwright, I. & Harley, S. L. (1998). The retrograde *P–T–t* path for low-pressure granulites from the Reynolds Range, central Australia: petrological constraints and implications for low-*P*/high-*T* metamorphism. *Journal of Metamorphic Geology* **16**, 511–529.

Cesare, B. (1994). Hercynite as the product of staurolite decomposition in the contact aureole of Vedrette-di-Ries, Eastern Alps, Italy. *Contributions to Mineralogy and Petrology* **116**, 239–246.

Chamberlain, C. P. & Rumble, D., III (1988). Thermal anomalies in a regional metamorphic terrane: an isotopic study of the role of fluids. *Journal of Petrology* **29**, 1215–1232.

Chamberlain, C. P. & Sonder, L. J. (1990). Heat-producing elements and the thermal and baric patterns of metamorphic belts. *Science* **250**, 763–769.

Chapman, D. S. & Furlong, K. P. (1992). Thermal state of the continental crust. In: Fountain, D. M., Arculus, R. & Kay, R. W. (eds) *Continental Lower Crust, Developments in Geotectonics, 23*. Amsterdam: Elsevier, pp. 179–199.

Cho, D.-L., Suzuki, K., Adachi, M. & Chwae, U. (1996). A preliminary CHIME age determination of monazite from metamorphic and granitic rocks in the Gyeonggi massif, Korea. *Journal of Earth and Planetary Sciences, Nagoya University* **43**, 49–65.

Cho, M. & Kim, J. (1993). Occurrence of kyanite in the Yongduri gneiss complex of the Chuncheon–Hongcheon area: its tectonometamorphic implication. *Journal of the Petrological Society of Korea* **2**, 1–8.

Cho, M., Kwon, S.-T., Ree, J.-H. & Nakamura, E. (1995). High-pressure amphibolite of the Imjingang Belt in the Yeoncheon–Cheongok area. *Journal of the Petrological Society of Korea* **4**, 1–19.

Cho, M., Lee, S. R., Yi, K. & Stern, R. (1999). Metamorphic and tectonic evolution of the Palaeoproterozoic granulites in the north-eastern Gyeonggi massif, South Korea. In: Miller, J. A. & Buick, I. S. (eds) *Orogenesis in the Outback, a Look at Cyclicity and Reactivation in Orogenic Belts. Geological Society of Australia Abstracts* **54**, 17.

Chough, S. K., Kwon, S.-T., Ree, J.-H. & Choi, D. K. (2000). Tectonic and sedimentary evolution of the Korean peninsula: a review and new view. *Earth-Science Reviews* **52**, 175–235.

Cluzel, D., Lee, B. J. & Cadet, J. P. (1991). Indosinian dextral ductile fault system and synkinematic plutonism in the southwest of the Ogcheon belt (South Korea). *Tectonophysics* **194**, 131–151.

Currie, K. L. & Gittins, J. (1988). Contrasting sapphirine parageneses from Wilson Lake, Labrador and their tectonic implications. *Journal of Metamorphic Geology* **6**, 603–622.

De Yoreo, J. J., Lux, D. R. & Guidotti, C. V. (1989). The role of crustal anatexis and magma migration in the thermal evolution of regions of thickened continental crust. In: Daly, J. S., Cliff, R. A. & Yardley, B. W. D. (eds) *Evolution of Metamorphic Belts. Geological Society, London, Special Publications* **43**, 187–202.

De Yoreo, J. J., Lux, D. R. & Guidotti, C. V. (1991). Thermal modeling of low-pressure/high-temperature metamorphic belts. *Tectonophysics* **188**, 209–238.

Eide, E. A., McWilliams, M. O. & Liou, J. G. (1994). $^{40}Ar/^{39}Ar$ geochronology and exhumation of high-pressure to ultra high-pressure metamorphic rocks in east–central China. *Geology* **22**, 601–604.

Ellis, D. J. (1987). Origin and evolution of granulites in normal and thickened crust. *Geology* **15**, 167–170.

Ellis, D. J. & Maboko, M. A. H. (1992). Precambrian tectonics and the physicochemical evolution of the continental crust. I. The gabbro–eclogite transition revisited. *Precambrian Research* **55**, 491–506.

England, P. C. & Thompson, A. B. (1984). Pressure–temperature–time paths of regional metamorphism, I. Heat transfer during the evolution of regions of thickened continental crust. *Journal of Petrology* **25**, 894–928.

Fitzsimons, I. C. W. & Harley, S. L. (1994). The influence of retrograde cation exchange on granulite *P–T* estimates and a convergence technique for the recovery of peak metamorphic conditions. *Journal of Petrology* **35**, 543–576.

Fountain, D. M. & Salisbury, M. H. (1981). Exposed cross-sections through the continental crust: implications for crustal structure, petrology and evolution. *Earth and Planetary Science Letters* **56**, 263–277.

Gerdes, A., Wörner, G. & Henk, A. (2000). Post-collisional granite generation and HT–LP metamorphism by radiogenic heating: the Variscan South Bohemian Batholith. *Journal of the Geological Society, London* **157**, 577–587.

Graham, C. M. & Powell, R. (1984). A garnet–hornblende geothermometer and application to the Pelona Schist, southern California. *Journal of Metamorphic Geology* **2**, 13–32.

Green, D. H. & Ringwood, A. E. (1967). An experimental investigation of the gabbro to eclogite transformation and its petrological applications. *Geochimica et Cosmochimica Acta* **31**, 767–833.

Harley, S. L. (1989). The origins of granulites: a metamorphic perspective. *Geological Magazine* **126**, 215–247.

Harley, S. L. (1992). Proterozoic granulite terranes. In: Condie, K. C. (ed.) *Proterozoic Crustal Evolution, Developments in Precambrian Geology, 10*. Amsterdam: Elsevier, pp. 301–359.

Harley, S. L. & Green, D. H. (1982). Garnet–orthopyroxene barometry for granulite and peridotites. *Nature* **300**, 697–701.

Hensen, B. J., Zhou, B. & Thost, D. E. (1995). Are reaction textures reliable guide to metamorphic histories? Timing constraints from garnet Sm–Nd chronology for 'decompression' textures in granulites from Sostrene Island, Prydz Bay, Antarctica. *Geological Journal* **30**, 261–271.

Holdaway, M. J. (1971). Stability of andalusite and the aluminum silicate phase diagrams. *American Journal of Science* **271**, 97–131.

Holdaway, M. J. & Lee, S. M. (1977). Fe–Mg cordierite in high grade pelitic rocks based on experimental and natural observations. *Contributions to Mineralogy and Petrology* **63**, 175–198.

Hollister, L. S. & Crawford, M. L. (1986). Melt-enhanced deformation: a major tectonic process. *Geology* **14**, 558–561.

Houseman, G. A., McKenzie, D. P. & Molnar, P. (1981). Convective instability of a thickened boundary layer and its relevance for the thermal evolution of continental convergent belts. *Journal of Geophysical Research* **86**, 6115–6132.

Huppert, H. E. & Sparks, S. J. (1988). The generation of granitic magmas by intrusion of basalt into continental crust. *Journal of Petrology* **29**, 599–624.

Ito, K. & Kennedy, C. (1971). An experimental study of the basalt–garnet granulite–eclogite transition. In: Heacock, J. G. (ed.) *The Structural and Physical Properties of the Earth's Crust. Geophysical Monograph Series, American Geophysical Union* **14**, 303–314.

Kay, R. W. & Kay, S. (1993). Delamination and delamination magmatism. *Tectonophysics* **219**, 177–189.

Kim, C.-B., Turek, A., Chang, H.-W., Park, Y.-S. & Ahn, K.-S. (1999). U–Pb zircon ages for Precambrian and Mesozoic plutonic rocks in the Seoul–Cheongju–Chooncheon area, Gyeonggi massif, Korea. *Geochemical Journal* **33**, 379–397.

Kim, J. N., Ree, J.-H., Kwon, S.-T., Park, Y., Choi, S. J. & Cheong, C.-S. (2000). The Kyonggi shear zone of the central Korean peninsula: late orogenic imprint of the North and South China collision. *Journal of Geology* **108**, 469–478.

Kohn, M. & Spear, F. S. (1990). Two new geobarometers for garnet amphibolites, with applications to southeastern Vermont. *American Mineralogist* **75**, 89–96.

Koziol, A. M. (1989). Recalibration of the garnet–plagioclase–Al_2SiO_5–quartz (GASP) geobarometer and application to natural parageneses. *EOS Transactions, American Geophysical Union* **70**, 493.

Kretz, R. (1983). Symbols for rock-forming minerals. *American Mineralogist* **68**, 277–279.

Leake, B. E. (1978). Nomenclature of amphiboles. *Mineralogical Magazine* **42**, 533–565.

LeBreton, N. & Thompson, A.B. (1988). Fluid-absent (dehydration) melting of biotite in metapelites in the early stages of crustal anatexis. *Contributions to Mineralogy and Petrology* **99**, 226–237.

Lee, D.-S. (ed.) (1987). *Geology of Korea*. Kyohaksa, S. Korea: Geological Society of Korea, 514 pp.

Lee, K. J. & Cho, M. (1992). Metamorphism of the Gyeonggi Massif in the Gapyeong–Cheongpyeong area. *Journal of the Petrological Society of Korea* **1**, 1–24.

Lee, S. R. & Cho, M. (1995). Tectonometamorphic evolution of the Chuncheon amphibolite, central Gyeonggi massif, South Korea. *Journal of Metamorphic Geology* **13**, 315–328.

Lee, S.R., Cho, M., Cheong, C.-S. & Park, K.-H. (1997). An early Proterozoic Sm–Nd age of mafic granulite from the Hwacheon area, South Korea. *Geosciences Journal* **1**, 136–142.

Lee, S. R., Cho, M., Yi, K. & Stern, R. (2000). Early Proterozoic granulites in central Korea: tectonic correlation with Chinese cratons. *Journal of Geology* **108**, 729–738.

Li, S. G., Chen, Y. Z., Cong, B. L., Zhang, Z. Q., Zhang, R. Y., Liu, D. L., Hart, S. R. & Ge, N. J. (1993). Collision of the North China and Yangtze blocks and formation of coesite-bearing eclogite: timing and processes. *Chemical Geology* **109**, 70–89.

Li, Z. X. (1994). Collision between the North and South China Blocks: a crustal-detachment model for suturing in the region east of the Tanlu fault. *Geology* **22**, 739–742.

Loosveld, R. J. H. & Etheridge, M. A. (1990). A model for low-pressure facies metamorphism during crustal thickening. *Journal of Metamorphic Geology* **8**, 257–267.

Moecher, D. P., Essene, E. J. & Anovitz, L. M. (1988). Calculation and application of clinopyroxene–garnet–plagioclase–quartz geobarometers. *Contributions to Mineralogy and Petrology* **100**, 92–106.

Mukhopadhyay, B. & Holdaway, M. J. (1993). Cordierite–garnet–sillimanite–quartz equilibrium: I. New experimental calibration in the system FeO–Al_2O_3–SiO_2–H_2O and certain P–T–X_{H_2O} relations. *Contributions to Mineralogy and Petrology* **116**, 462–472.

Oxburgh, E. R. (1990). Some thermal aspects of granulite history. In: Vielzeuf, D. & Vidal, Ph. (eds) *Granulites and Crustal Evolution. NATO ASI Series* **311**, 569–580.

Patiño Douce, A. E., Humphreys, D. & Johnston, A. D. (1990). Anatexis and metamorphism in tectonically thickened continental crust exemplified by the Sevier hinterland, western North America. *Earth and Planetary Science Letters* **97**, 290–315.

Perchuk, L. L. & Lavren'teva, I. V. (1983). Experimental investigation of exchange equilibria in the system cordierite–garnet–biotite. In: Saxena, S. K. (ed.) *Advances in Physical Geochemistry, Kinetics and Equilibrium in Mineral Reactions, 3*. New York: Springer, pp. 199–239.

Percival, J. A., Fountain, D. M. & Salisbury, M. H. (1992). Exposed crustal cross sections as windows on the lower crust. In: Fountain, D. M., Arculus, R. & Kay, R. W. (eds) *Continental Lower Crust, Developments in Geotectonics, 23*. Amsterdam: Elsevier, pp. 317–362.

Phillips, G. N. (1980). Water activity changes across an amphibolite–granulite-facies transition, Broken Hill, Australia. *Contributions to Mineralogy and Petrology* **75**, 377–386.

Ree, J.-H., Cho, M., Kwon, S.-T. & Nakamura, E. (1996). Possible eastward extension of Chinese collision belt in South Korea: the Imjingang Belt. *Geology* **24**, 1071–1074.

Rudnick, R. L. (1995). Making continental crust. *Nature* **378**, 571–578.

Sandiford, M. (1985). Metamorphic evolution of granulites at Fyfe Hills: implications for Archean crustal thickness. *Journal of Metamorphic Geology* **3**, 155–178.

Sandiford, M. & Powell, R. (1990). Some isostatic and thermal consequences of the vertical strain geometry in convergent orogens. *Earth and Planetary Science Letters* **98**, 154–165.

Sandiford, M. & Powell, R. (1991). Some remarks on high-temperature–low-pressure metamorphism in convergent orogens. *Journal of Metamorphic Geology* **9**, 333–340.

Sawyer, E. W. (1994). Melt segregation in the continental crust. *Geology* **22**, 1019–1022.

Schenk, V. (1984). Petrology of felsic granulites, metapelites, metabasics, ultramafics and metacarbonates from southern Calabria (Italy): prograde metamorphism, uplift and cooling of a former lower crust. *Journal of Petrology* **25**, 255–298.

Stevens, G., Clemens, J. D. & Droop, G. T. R. (1997). Melt production during granulite-facies anatexis—experimental data from primitive metasedimentary protoliths. *Contributions to Mineralogy and Petrology* **128**, 352–370.

Stoddard, E. F. (1979). Zinc-rich hercynite in high-grade metamorphic rocks: a product of the dehydration of staurolite. *American Mineralogist* **64**, 736–741.

Suzuki, K. & Adachi, M. (1999). CHIME ages of orthogneisses and paragneisses from the Gyeonggi Massif, Korean Peninsula. *Japanese Association of Mineralogical, Petrological and Economic Geologists, Abstract Volume*, D14.

Taylor, S. R. & McLennan, S. M. (1985). *The Continental Crust: its Composition and Evolution*. Oxford: Blackwell.

Thompson, A. B. (1990). Heat, fluids and melting in the granulite facies. In: Vielzeuf, D. & Vidal, Ph. (eds) *Granulites and Crustal Evolution. NATO ASI Series* **311**, 37–57.

Thompson, A. B. & Connolly, A. D. (1995). Melting of the continental crust: some thermal and petrological constraints on anatexis in continental collision zones and other tectonic settings. *Journal of Geophysical Research* **100**, 15565–15579.

Thompson, A. B. & Ridley, J. R. (1987). Pressure–temperature–time (P–T–t) histories of orogenic belts. *Philosophical Transactions of the Royal Society of London, Series A* **321**, 27–45.

Thompson, P. H. (1989). Moderate overthickening of thinned sialic crust and the origin of granitic magmatism and regional metamorphism in low P–high T terranes. *Geology* **17**, 520–523.

Vernon, R. H. (1996). Problems with inferring P–T–t paths in low-P granulite facies rocks. *Journal of Metamorphic Geology* **14**, 143–153.

Vielzeuf, D. & Holloway, J. R. (1988). Experimental determination of the fluid-absent melting relations in the pelitic system—consequences for crustal differentiation. *Contributions to Mineralogy and Petrology* **98**, 257–276.

Wells, P. R. A. (1980). Thermal models for the magmatic accretion and subsequent metamorphism of continental crust. *Earth and Planetary Science Letters* **46**, 253–265.

Wickham, S. M. (1987). The segregation and emplacement of granitic magmas. *Journal of the Geological Society, London* **144**, 281–297.

Yi, K. (1998). Reaction textures and *P–T* paths in the Hwacheon granulite complex, South Korea. M.Sc. Thesis, Seoul National University, 87 pp.

Yi, K., Cho, M., Lee, S. R. & Wintsch, R. P. (2001). Dating polymetamorphism in a granulite–amphibolite: Early Proterozoic and Permo-Triassic chemical ages of monazite. *Northeastern Regional Meeting, Geological Society of America, Abstract Volume*, A-82.

Yin, A. & Nie, S. (1993). An indentation model for the North and South China collision and the development of the Tan-Lu and Honam fault systems, eastern Asia. *Tectonics* **12**, 801–813.

Young, E. D., Anderson, J. L., Clarke, H. S. & Thomas, W. M. (1989). Petrology of biotite–cordierite–garnet gneiss of the McCullough Range, Nevada I. Evidence for Proterozoic low-pressure fluid-absent granulite-grade metamorphism in the southern Cordillera. *Journal of Petrology* **30**, 39–60.

Zhao, G., Wilde, S. A., Cawood, P. A. & Sun, M. (2001). Archean blocks and their boundaries in the North China Craton: lithological, geochemical, structural and *P–T* path constraints and tectonic evolution. *Precambrian Research* **107**, 45–73.